Monthly Notices of the ROYAL ASTRONOMICAL SOCIETY

MNRAS **525,** 5795–5812 (2023) https://doi.org/10.1093/mnras/stad2530
Advance Access publication 2023 September 1

Revealing AGNs through TESS variability

Helena P. Treiber [1,2★] Jason T. Hinkle [1] Michael M. Fausnaugh,[3] Benjamin J. Shappee [1] Christopher S. Kochanek [4] Patrick J. Vallely [4] Katie Auchettl [5,6] Thomas W.-S. Holoien [7†] Anna V. Payne [1‡] and Xinyu Dai [8]

[1]*Institute for Astronomy, University of Hawai'i, 2680 Woodlawn Dr., Honolulu, HI 96822, USA*
[2]*Department of Physics and Astronomy, Amherst College, C025 New Science Center, 25 East Dr., Amherst, MA 01002-5000, USA*
[3]*Department of Physics and Kavli Institute for Astrophysics and Space Research, Massachusetts Institute of Technology, Cambridge, MA 02139, USA*
[4]*Department of Astronomy, The Ohio State University, 140 West 18th Avenue, Columbus, OH 43210, USA*
[5]*School of Physics, University of Melbourne, Victoria 3010, Australia*
[6]*Centre for Cosmology and Astroparticle Physics, The Ohio State University, 191 W. Woodruff Avenue, Columbus, OH 43210, USA*
[7]*The Observatories of the Carnegie Institution for Science, 813 Santa Barbara Street, Pasadena, CA 91101, USA*
[8]*Homer L. Dodge Department of Physics and Astronomy, University of Oklahoma, Norman, OK 73019, USA*

Accepted 2023 August 16. Received 2023 August 10; in original form 2022 October 19

ABSTRACT

We used Transiting Exoplanet Survey Satellite (TESS) data to identify 29 candidate active galactic nuclei (AGNs) through their optical variability. The high-cadence, high-precision TESS light curves present an opportunity for the identification of AGNs, including those not selected through other methods. Of the candidates, we found that 18 have either previously been identified as AGNs in the literature or could have been selected based on emission-line diagnostics, mid-IR colours, or X-ray luminosity. AGNs in low-mass galaxies offer a unique window into supermassive black hole and galaxy co-evolution and 8 of the 29 candidates have estimated black hole masses $\lesssim 10^6\,M_\odot$. The low-mass galaxies NGC 4395 and NGC 4449 are two of our five 'high-confidence' candidates. Since our initial sample largely draws from just nine TESS sectors, we expect to identify at least ∼45 more candidates in the TESS primary and extended mission data sets, of which ∼60 per cent will be new AGNs and ∼20 per cent will be in low-mass galaxies.

Key words: black hole physics – surveys – galaxies: active – galaxies: dwarf.

1 INTRODUCTION

Most massive galaxies contain supermassive black holes (SMBHs, Kormendy & Richstone 1995; Richstone et al. 1998). Active galactic nuclei (AGNs), where the SMBH is accreting, are seen in 1–5 per cent of galaxies in the local universe (e.g. Ho 2008; Haggard et al. 2010; Lacerda et al. 2020; Mishra et al. 2021; Yuk et al. 2022). AGNs inform our understanding of galaxy and SMBH co-evolution and provide a detailed look at the physics of accretion (see Heckman & Best 2014, for a review).

AGNs are commonly selected using emission-line diagnostics (e.g. Baldwin, Phillips & Terlevich 1981; Veilleux & Osterbrock 1987; Kewley et al. 2006; Cid Fernandes et al. 2011, see Section 5.2), colour (e.g. Koo & Kron 1988; Fan 1999; Richards et al. 2001; Lacy et al. 2004; Stern et al. 2012; Assef et al. 2013, see Section 5.4), radio luminosity (e.g. Baade & Minkowski 1954; Tadhunter 2016), and X-ray luminosity (e.g. Elvis et al. 1978; Mendez et al. 2013, see Section 5.3). These methods are sensitive to different AGN populations (e.g. Hickox et al. 2009). For example, although spectroscopic methods can be used in the identification of AGNs in low-mass galaxies, the lower metallicity and higher star formation rates in these galaxies can complicate line ratio diagnostics (e.g. Trump et al. 2015).

A key feature of AGNs is their stochastic variability across the electromagnetic spectrum. As a result, variability selection is one of the most promising ways of identifying actively accreting BHs. In particular, emission-line diagnostics miss the majority of variability-selected AGNs in low-mass galaxies (Baldassare, Geha & Greene 2020; Burke et al. 2021; Latimer et al. 2021; Ward et al. 2022; Yuk et al. 2022; Burke et al. 2023). The fraction of low-mass galaxies with an AGN (i.e. the active fraction) is not well constrained, but has been predicted to be lower than at higher masses (e.g. Pacucci, Mezcua & Regan 2021; Burke et al. 2023). In addition to enlarging the known population of low-mass AGNs, the light curves from variability selection can be used to probe the physics of accretion. In particular, photometric reverberation mapping can be used to measure accretion disc sizes (e.g. Haas et al. 2011; Chelouche & Daniel 2012; Edri et al. 2012; Shappee et al. 2014; Fausnaugh et al. 2018).

AGN variability is often described by a damped random walk (DRW; e.g. Kelly, Bechtold & Siemiginowska 2009; Kozłowski et al. 2010; MacLeod et al. 2010). MacLeod et al. (2010), Kelly et al. (2009), and Burke et al. (2020) all find that the characteristic timescale of the DRW model ($\tau_{\rm DRW}$) becomes shorter for lower mass

★ E-mail: lena.treiber@princeton.edu
† NHFP Einstein Fellow.
‡ NASA Graduate Fellow.

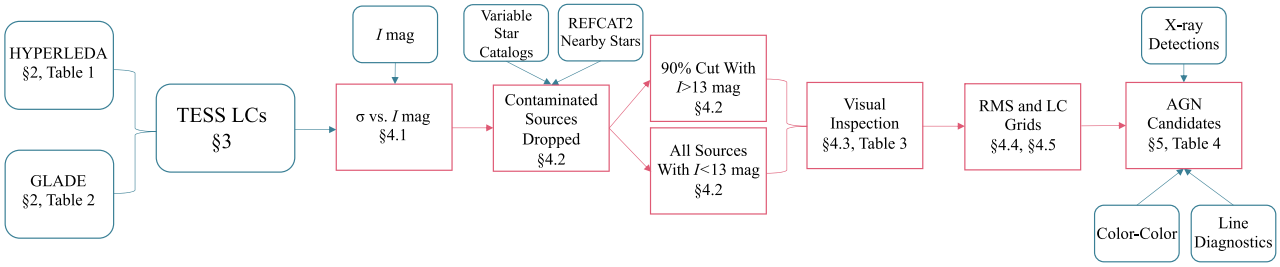

Figure 1. Flow chart outlining steps from sample selection to AGN candidate identification. Steps that introduce data are shown with rounded blue outlines, while cuts are described in pink rectangles.

SMBHs. Regardless of the efficacy of the DRW model, non-beamed AGN emission is unlikely to vary faster than the light-crossing time of the accretion disc, which is larger for a higher mass black hole (e.g. Xie et al. 2005).

Thanks to the high cadence of the Transiting Exoplanet Survey Satellite[1] (TESS; Ricker et al. 2014), we can now search for optical variability on ∼hour time-scales. Burke et al. (2020) showed that the well-known Seyfert 1 in the dwarf galaxy NGC 4395 (Filippenko & Sargent 1989) optically varies with a $\tau_{\rm DRW} \sim 2.5$ d. This result suggests that the cadence, precision, and all-sky coverage of TESS should make it a useful tool in the study of variability from AGNs in low-mass galaxies. Furthermore, the $\tau_{\rm DRW}$ of NGC 4395 indicates that the $\tau_{\rm DRW}$−$M_{\rm BH}$ relation extends several orders of magnitude down to this $\sim 10^5\,M_\odot$ BH. Burke et al. (2021) corroborated this result by adding to the relation several AGNs with variability observed by other optical telescopes.

In this paper, we search for AGNs using TESS light curves. During its 2-yr prime mission, the main goal of TESS was to identify transiting exoplanets around M dwarf stars (e.g. Gilbert et al. 2020). The resulting photometric precision and high cadence make TESS an excellent tool for a much broader range of time-domain studies (e.g. Holoien et al. 2019; Fausnaugh et al. 2021; Mishra et al. 2021; Payne et al. 2021; Vallely et al. 2021; Zeldes et al. 2021; Hinkle et al. 2022; Way et al. 2022; Payne et al. 2022a; Hinkle et al. 2023). Using four 24 × 24 deg^2 FOV cameras, TESS repeatedly images one of 26 sectors (13 per hemisphere) for ∼27 d at a time, with a target photometric precision ranging from ∼50 ppm at I magnitude of 6 to ∼1 per cent for $I = 16$ mag. (Ricker et al. 2014). The wide 600–1000-nm bandpass is centred on the Cousins I band, with an effective wavelength of 745.3 nm (Ricker et al. 2014; Rodrigo & Solano 2020). We focus on the mission's first 2 yr, when TESS took full-frame images (FFIs) every 30 min.

In Fig. 1, we outline the steps of our search for AGNs using TESS. In Section 2, we explain our sample selection. We summarize the steps involved in TESS light curve generation in Section 3. We detail our methodology to account for stellar contamination and systematics, such as scattered light and spacecraft jitter (e.g. Vanderspek et al. 2018). Following variability cuts, we present the 29 AGN candidates in Section 4. In Section 5, we investigate archival data for the 29 AGN candidates. We demonstrate that up to 38 per cent of the AGN candidates can only be selected using variability. We assume the same cosmological parameters as HyperLEDA (Makarov et al. 2014) to convert between redshift and distance: $H_0 = 70\,{\rm km\,s^{-1}\,Mpc^{-1}}$, $\Omega_{\rm M} = 0.27$, and $\Omega_\Lambda = 0.73$.

2 THE SAMPLE

Our sample comes from two galaxy catalogues using different sets of selection criteria: HyperLEDA (Makarov et al. 2014), limited by TESS sector (2, 3, 4, 5, 6, 7, 19, 20, and 21) but not mass, and the Galaxy List for the Advanced Detector Era (GLADE, Dálya et al. 2018), limited by inferred mass ($M_{\rm BH} \lesssim 10^7 M_\odot$) but not sector. We used the catalogued coordinates to perform forced photometry (Section 3). Because statistical noise dominates the TESS light curves of fainter galaxies, we only included galaxies with $I < 16$ mag.

The majority of our sample consists of galaxies catalogued in HyperLEDA.[2] By compiling and processing several galaxy catalogues, HyperLEDA maintains a database of ∼5 million extragalactic objects. The TESS light curves of the 137 695 HyperLEDA sources in our sample were generated along with galaxies as faint as $I = 20$ mag, using forced photometry and the techniques of Fausnaugh et al. (2021) (see Section 3). The light curves from the first few sectors showed clear systematics from scattered light, particularly for the fainter sources excluded from our sample (i.e. $I > 16$ mag), for about half of each year (Vanderspek et al. 2018). Therefore, besides the first few sectors, we only consider the light curves for sectors where this scattered light contribution is relatively low: 5, 6, 7, 19, 20, and 21. Thus, the sample consists of sources in nine sectors (2, 3, 4, 5, 6, 7, 19, 20, and 21). Table 1 includes TESS-related information and relevant galaxy properties catalogued in HyperLEDA.

For the GLADE sample, we considered galaxies likely to have lower mass central BHs ($M_{\rm BH} \lesssim 10^7 M_\odot$) based on their absolute K magnitudes. We chose to use GLADE because it combines data from several other catalogues. In addition to the mass cut, we limited the redshift to $0.0001 < z < 0.5$ to further confirm that stars and higher redshift quasars do not contaminate the sample. The lower bound on z removed 38 sources but the upper bound had no effect on the sample. GLADE does not report I-band magnitudes. However, using GLADE galaxies also in the HyperLEDA catalogue, we found that

$$I = J \times 0.91 + 1.99\ {\rm mag} \quad (1)$$

was a reasonable proxy to use for our $I \lesssim 16$ selection limit. Although 5676 galaxies in GLADE satisfied our selection parameters, 1310 of them either fell between pointings in the TESS primary mission or in the eight-pixel buffer at the edge of the detector. Table 2 includes the 4366 low-mass sources from GLADE for which we could generate TESS primary mission light curves.

We estimated black hole masses for both the HyperLEDA and GLADE samples using equation (14) from Graham (2007), which has a scatter of ∼0.33 dex. Although there is a comparable relation reported in Graham & Scott (2013), its increased scatter makes the

[1] https://tess.mit.edu/observations/

[2] http://leda.univ-lyon1.fr/

Table 1. HyperLEDA sample.

Name	RA (°)	Dec. (°)	Number of sectors	*I* Vega mag	K_{abs} Vega mag	$\log(M_{BH}/M_\odot)$
PGC 124374	0.001	−41.423	1	15.0	−23.9	8.3
PGC 520795	0.001	−45.954	1	15.5	–	–
PGC 143101	0.003	−59.013	1	14.9	–	–
PGC 130936	0.004	−40.903	1	13.6	−25.2	8.7
PGC 124869	0.010	−38.894	1	15.9	−23.4	8.1
PGC 143105	0.013	−34.064	1	15.3	−23.4	8.1
PGC 598724	0.014	−39.388	1	15.7	–	–
PGC 129171	0.017	−49.281	1	14.6	−23.3	8.0
PGC 445008	0.018	−52.366	1	14.9	−25.4	8.8
PGC 407967	0.024	−55.578	1	15.4	−25.8	9.0

Note. Identifying information and key values for the 137 695 galaxies in the HyperLEDA sample. Columns 1, 2, 3, 5, and 6 are taken from HyperLEDA, where column 6, which is total galaxy absolute *K* mag, uses catalogued *K* mag and distance modulus without any corrections. Column 4 only includes sectors used for our HyperLEDA sample: 2, 3, 4, 5, 6, 7, 19, 20, and 21. Column 7 values are estimated using column 6 and equation (14) from Graham (2007). Only a section of the table is shown here to demonstrate table formatting; the rest, sorted by right ascension, can be found in the ancillary files.

Table 2. GLADE sample.

Name	RA (°)	Dec. (°)	Number of sectors	*I* Vega mag	K_{abs} Vega mag	$\log(M_{BH}/M_\odot)$
00001173 + 7027274	0.049	70.458	4	15.8	−19.4	6.6
00001208 + 6028060	0.050	60.468	3	15.4	−18.1	6.1
00002106 + 6639495	0.088	66.664	3	15.8	−16.5	5.5
00003684 + 5813001	0.154	58.217	2	15.6	−18.2	6.1
00004629 + 7010344	0.193	70.176	4	15.3	−18.6	6.3
00010116 + 6607289	0.255	66.125	3	15.5	−16.9	5.7
00010881 + 7138091	0.287	71.636	4	15.3	−19.8	6.7
00013579 + 6131240	0.399	61.523	2	15.3	−19.6	6.7
00020922 + 7024328	0.538	70.409	4	15.9	−19.1	6.5
00022239 + 5852447	0.593	58.879	3	15.7	−18.6	6.3

Note. TESS information and galaxy properties for the 4366 galaxies in the GLADE sample. The names are from the 2MASS XSC catalogue (Skrutskie et al. 2006) and are preceded by 2MASX J. Columns 2–4 are from GLADE, with column 4 using catalogued distances and *K* magnitudes. We estimate values for column 3 using catalogued *J* magnitudes in GLADE and equation (1). For column 5 estimates, we use column 4 and equation (14) from Graham (2007). Only a section of the table is shown here; the rest can be found in the ancillary files.

best-fitting relation highly dependent on the chosen fitting approach. For the GLADE sample, we cut at M_{BH} of $10^7\,M_\odot$ to restrict the sample to low-mass black holes. This empirical correlation used galaxies with *K*-band measurements for the spheroidal component of the galaxy and independently estimated black hole masses. However, at this stage, we used the Graham (2007) relation on the total galaxy absolute *K*-band magnitudes for two reasons. First, the majority of galaxies in the GLADE sample have only photometric redshifts, making the distances and resulting BH mass estimates significantly uncertain ($\gtrsim$1 dex), especially at low redshift (Bilicki et al. 2014; Dálya et al. 2018). Second, we lack morphological information for all of the GLADE and most of the HyperLEDA galaxies. In addition, we note that these *K*-band magnitudes are not *K*-corrected. However, even at our redshift upper limit of $z = 0.5$, the *K* mag *K*-correction of $\sim$−0.6 mag (e.g. Blanton & Roweis 2007; Chilingarian, Melchior & Zolotukhin 2010) would only alter the corresponding $\log(M_{BH}/M_\odot)$ estimate by $\sim$0.2. We treat the BH mass estimates using the Graham (2007) relation as approximate upper limits.

For the final AGN candidates, we obtained morphological classifications and either redshift-independent distances or spectroscopic redshifts to re-estimate the candidate BH masses (see Section 4.6). For four of the five candidates from the GLADE sample, the new estimate yielded lower BH mass estimates by over an order of magnitude. The major driver of this change was the incorporation of morphologies. The distributions of the samples in *I* mag, redshift, and estimated black hole mass are shown in Fig. 2. There are some M_{BH} estimates under $10^4\,M_\odot$ but these estimates seem unphysical and are instead likely a result of underestimated distances for some of the closest sources in the GLADE sample. One can compare these sample histograms (Fig. 2) to the comparable ones for the final 29 AGN candidates in Fig. 17.

3 TESS LIGHT CURVES

Following the methods presented in Fausnaugh et al. (2021), we produced prime mission (Sectors 1 − 26) TESS light curves. We summarize the steps here. Using reference images built from 20 FFIs, we employed the difference imaging technique of Alard & Lupton (1998) and Alard (2000) through the `ISIS` package. These were then scaled in flux and PSF structure and subtracted from each FFI along with a 2D polynomial model of the sky. The resulting subtracted images still have many TESS-related systematic features (e.g. the 'straps' and various reflection features), which we remove

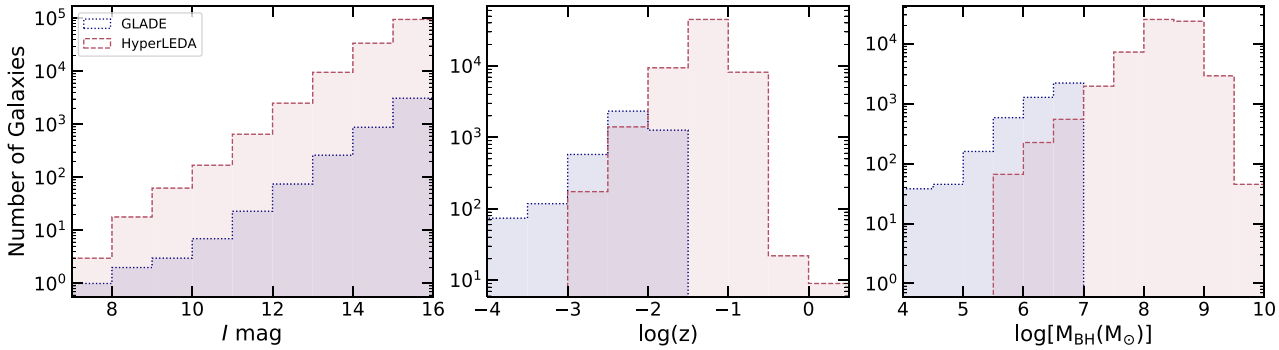

Figure 2. Histograms of the apparent *I*-band magnitude, redshift, and estimated black hole mass for galaxies in the HyperLEDA and GLADE samples. GLADE galaxies are shown by a navy dotted line and HyperLEDA uses a pink-dashed line. There are a few mass estimates below 10^4 M_{BH} for close sources with no redshift-independent distance measurements.

using median filters to build a model of the residual backgrounds. The light curves for each source are then extracted.

For sources that passed visual inspection and the root mean square (RMS) check (see Sections 4.4 and 4.5), we also generated light curves according to the techniques outlined in Vallely et al. (2021). This approach is similar to that of Fausnaugh et al. (2021), but analyzes a local patch around the target source rather than the full FFI and uses a more involved treatment of various TESS artefacts. Having light curves from both pipelines allows us to check whether the same AGN-like variability pattern is present in both pipelines.

4 CANDIDATE AGN IDENTIFICATION

In this section, we describe how we identified the AGN candidates from the sample of 142 061 galaxies. First, as described in Section 4.1, we examined the typical light curve magnitude dispersion as a function of magnitude to separate physical variability from noise. Then, we identified nearby stars and calculated whether their estimated variability could account for the apparent variability of the galaxy (Section 4.2). Next, we inspected the remaining light curves for AGN-like variability (Section 4.3). The candidates that passed the visual check are listed in Table 3. Finally, in Sections 4.4 and 4.5, we describe the further steps we took to check for contamination using inspection of the RMS images and the light curves of nearby pixels.

4.1 Sigma versus magnitude

To differentiate between noise and physical variability, we examine the standard deviation of the light curves in magnitude as a function of the *I* magnitude (Fig. 3). Due to crowding and the large TESS pixels, it is difficult to accurately measure a source's mean flux from the TESS data. We used the catalogued *I* magnitude because the TESS filter is roughly centred on the *I* band.

We converted the *I*-band magnitude to TESS counts per second using the TESS filter zero point of 20.44 mag (Vanderspek et al. 2018) and then added the counts from the subtracted light curve assuming an average FFI exposure time of 1425.6 seconds (instead of the full 30 min) to account for the exposure time lost due to cosmic-ray removal. We then converted back to magnitudes to have a reasonable approximation of a TESS *T*-band (or *I*-band) light curve.

To ensure that the estimated standard deviation was not dominated by TESS systematics, we trimmed each light curve of the commonly problematic parts of a sector. In particular, there are often unphysical jumps in the count rate at either end of a sector, so we took out the first and last 1.5 d. There is also a brief interruption in data collection as TESS passes the mid-sector perigee and sends data to the ground. We trimmed 3 d on either side of this downlink because the re-orientation of the spacecraft leads to temperature changes that affect the light curves. This trimming leaves typical light curves with 18 total days of data and a cadence of 30 min. The temperature effects can seem to impact the light curves on time-scales ranging from 0 to 8 d, sometimes longer than the trimmed duration. Because the cut is often conservative, we only used the trimmed versions to compute the standard deviation of the light curves and keep these regions for visual inspection.

4.2 Contamination by nearby stars

Next, we identified galaxy light curves that may be contaminated by nearby variable stars. We first queried the ATLAS-VAR catalogue[3] (Heinze et al. 2018) and the ASAS-SN Variable Stars Database,[4] which has fewer stars but better coverage of the Southern hemisphere (Jayasinghe et al. 2019, 2021). We identified stars within 4 arcmin (∼11 TESS pixels) of the galaxies because the model TESS Pixel Response Function[5] (PRF, Vanderspek et al. 2018) goes to zero at 9 pixels. Using a typical PRF and the catalogued variability amplitude, we computed the contribution the variable star would make to the measured flux of the galaxy. We added this 'variable flux' to the estimated Poisson noise in quadrature to obtain an estimate of variability in the galaxy light curve that can be attributed to the star. If this value was greater than the light curve standard deviation, we flagged this source as potentially dominated by stellar variability. This step removed 10 805 galaxies.

Ground-based variable star databases usually catalogue stars that vary by $\gtrsim 1$ per cent, but TESS is sensitive to lower variability amplitudes. Therefore, we repeated the contamination procedure by assigning each nearby ATLAS REFCAT2 (Tonry et al. 2018) star a 1 per cent variability amplitude (e.g. Huber et al. 2011; McQuillan et al. 2014; Yu et al. 2020). Of the sources not already flagged using ATLAS-VAR and ASAS-SN, another 29 per cent are considered contaminated, as shown in Fig. 4. Thus, a total of 49 133 sources are deemed contaminated using these three catalogues. Each of these

[3] https://archive.stsci.edu/hlsp/atlas-var
[4] https://asas-sn.osu.edu/variables
[5] https://archive.stsci.edu/missions/tess/models/prf_fitsfiles/

Table 3. AGN candidates following visual inspection.

Name	RA (°)	Dec. (°)	Number of sectors	*I* Vega mag	log($M_{BH}/M_{\odot}$)	Source outcome
PGC 780808	0.102	− 25.272	1	15.8	8.3	RMS PRF off-centre
PGC 651376	2.315	− 35.246	1	14.7	8.3	RMS PRF off-centre
NGC 0055	3.723	− 39.197	1	8.7	6.9	candidate
PGC 841750	3.968	− 20.440	1	15.5	–	RMS PRF off-centre
PGC 979064	4.708	− 10.369	1	15.9	–	RMS PRF off-centre
PGC 1029922	5.467	− 6.692	1	15.9	–	RMS PRF off-centre
PGC 651468	7.094	− 35.240	1	15.5	–	RMS PRF off-centre
NGC 0157	8.695	− 8.396	1	9.5	8.3	Candidate
PGC 143644	9.021	− 7.768	1	13.9	8.6	RMS PRF off-centre
NGC 1247	48.060	− 10.481	1	11.3	8.6	Grid not AGN-like

Note. Sources with AGN-like variability identified through visual inspection. Only a section of the table is shown here to demonstrate table formatting; the rest of the 258 sources can be found in the ancillary files. We label sources with 'candidate' in the Source Outcome column if they are final AGN candidates. Those that were cut during the RMS check (Section 4.4) are labelled 'RMS PRF off-centre'. We use 'grid not AGN-like' to describe the outcome of sources that pass RMS but not the light curve grid (Section 4.5).

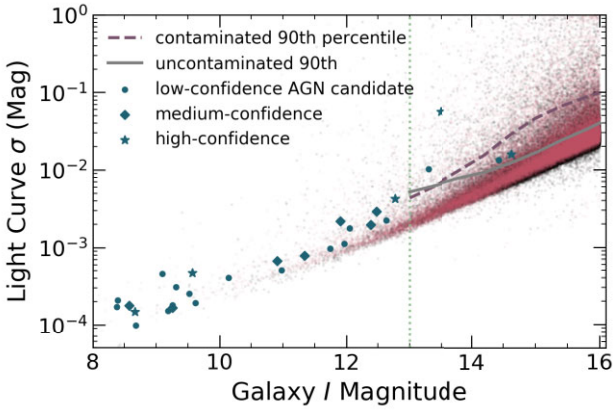

Figure 3. Standard deviation versus magnitude for the whole sample, illustrating the increasing noise at fainter magnitudes. Sources found to be contaminated prior to visual inspection are shown in pink, and the rest are in black. The purple-dashed line follows the 90th percentile for the contaminated sources only, while the grey solid curve follows the uncontaminated 90th percentile. Below 13th mag (shown by the vertical dotted line), we inspect all uncontaminated sources. Final AGN candidates are marked. The candidate with the highest light curve σ is ESO 362–021 (Fig. 10), which is a known blazar.

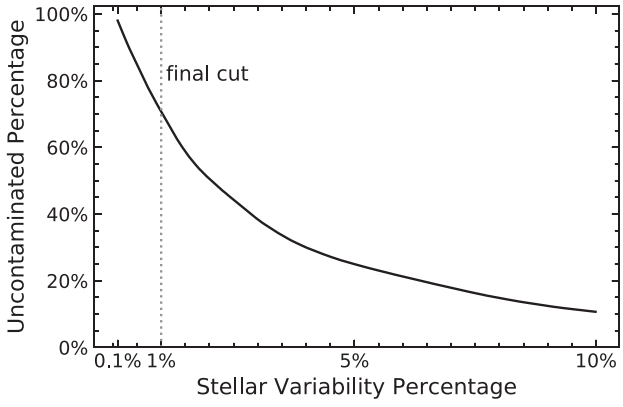

Figure 4. Percentage of sources that we consider 'uncontaminated' by nearby stars catalogued in ATLAS REFCAT2 as a function of the estimated stellar variability percentage attributed to the stars. We only include sources that we consider uncontaminated by the known variable stars in ATLAS-VAR and ASAS-SN. We cut at the reasonable value of 1 per cent variability (e.g. Huber et al. 2011; McQuillan, Mazeh & Aigrain 2014; Yu et al. 2020), yielding an 'uncontaminated percentage' of 71 per cent. Ultimately, though, stellar contamination remains in a significant fraction of the galaxy light curves that are not flagged at this stage.

sources is shown in pink in Fig. 4.1 and we show the 'uncontaminated' sources in black. A visual inspection of sources *without* this contamination filtering confirms that a significant majority of sources that appear to have AGN-like variability are in fact contaminated.

4.3 Visual inspection of light curves

Of the sources not cut in the first contamination filtering (Section 4.2), we visually inspected the 10 per cent of galaxies that are most variable (i.e. those above the grey curve in Fig. 4.1) as well as the 899 sources with $I < 13$ mag. We looked for aperiodic variability with peaks of varying amplitude. Because the initial contamination filtering does not robustly remove stellar contamination, we focused on a search for this typical form of AGN variability. However, we note that there is evidence in several galactic nuclei of (quasi-)periodic variability, which is often proposed to originate from an SMBH binary (e.g. Komossa 2006; Graham et al. 2015; Charisi et al. 2016; Liu et al. 2019), or, as in the case of ASASSN-14ko, a repeating partial tidal disruption event (Payne et al. 2021; Tucker et al. 2021; Payne et al. 2022a, b). Using our methodology, it is overwhelmingly likely that periodicity in a light curve in visual inspection is stellar. However, searches for periodic AGN variability will be feasible in future studies that use RMS images (see Section 4.4) or other robust forms of contamination filtering early on.

We simultaneously examined the background model, because the presence of strong common trends, especially when the galaxy is not bright enough for the wings of the galaxy's PRF to affect nearby TESS pixels, implies that a star has contaminated both the galaxy PRF and the background.

We rejected a source during visual inspection if (1) the light curve was consistent with noise with no clear evidence of variability, (2) the light curve appeared clearly consistent with stellar variability because of a periodicity or a strong correlation between the light curve and the background model, or (3) the light curve variability resembled TESS

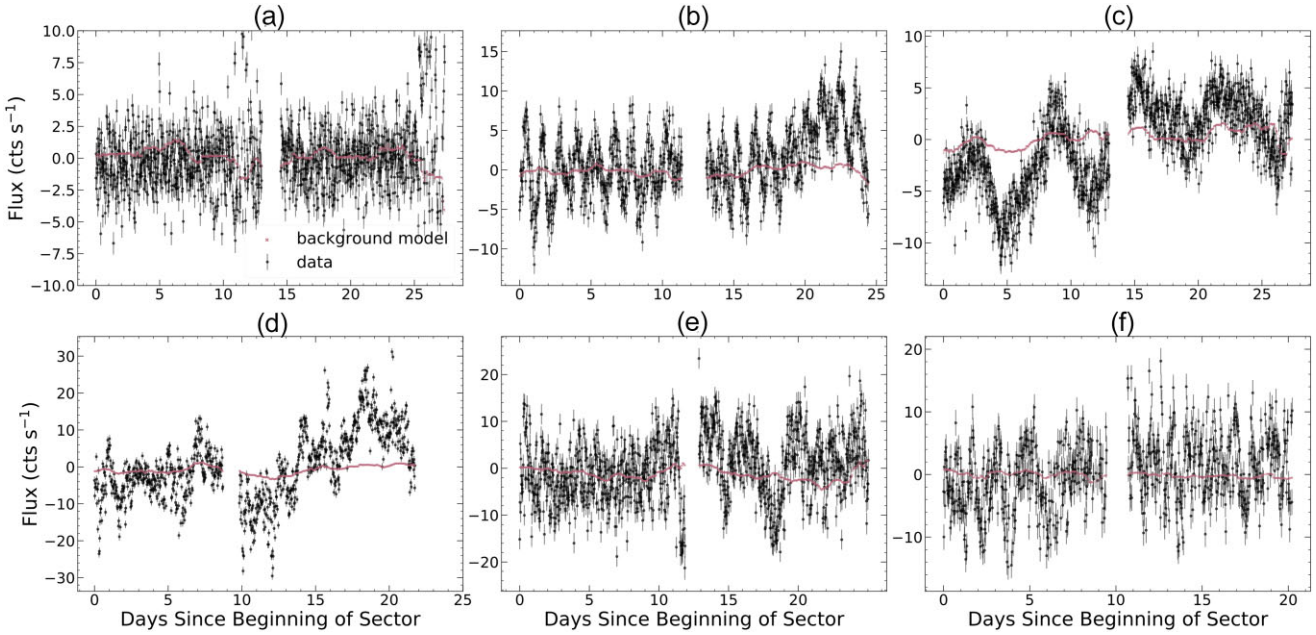

Figure 5. Representative visually inspected light curves are shown in black, while the background model, which has already been subtracted, is shown in pink. Panel (a): The light curve is consistent with noise. Panel (b): The consistent periodicity suggests that this source is likely contaminated by a nearby variable star. Panel (c): The light curve has too much correlation with the background model to be chosen as a candidate. Panel (d): This object was cut before visual inspection due to contamination, and is included to illustrate the importance of this step. Panel (e): Although NGC 6503 passed visual inspection, we later rejected it because its grid of neighbouring light curves showed evidence for systematics that could explain the observed variability. Panel (f): NGC 0157 is selected as a candidate. The final contamination checks give this source 'low' confidence. The presence of some correlation with the background model is not worrisome, since NGC 0157 is ∼4 mag brighter than the source shown in Panel (c), while the background model has a much lower relative amplitude.

systematics rather than physical variability (e.g. all the significant variability was near the sector downlink, especially in cases where the trimming for the standard deviation measurement is insufficiently robust for cutting out downlink-related temperature effects in the light curve). We show examples of these various cases in Fig. 5. Evolved stars also have quasi-periodic variability with changing peak amplitudes (e.g. Auge et al. 2020), so we relied on later checks to distinguish between AGNs and irregularly varying stars. The sources that we identified as having AGN-like variability are included in Table 3, but further checks for contamination (Sections 4.4 and 4.5) revealed that the large majority of the visually inspected sources are also contaminated, showing that the contamination filtering in Section 4.2 was not sufficiently robust.

4.4 RMS images

For the 258 galaxies listed in Table 3 that passed the visual inspection step (Section 4.3), we next examined the corresponding reference image and an RMS image defined by the RMS of the subtracted images. Peaks in the RMS image correspond to the positions of variable sources and for a variable AGN should coincide with the position of the galaxy. We therefore rejected a source when there was an offset. Also complicating some RMS images were overlapping variable sources and oddly shaped PRFs.

We show examples of the RMS images in Fig. 6. The top row, which shows the images for ESO 362–021, demonstrates the utility of the RMS images. ESO 362–021 is not the brightest source in the region, but the galaxy is clearly the only variable source in the RMS image. On the other hand, NGC 1365, in the bottom row of Fig. 6, has a complicated RMS image. Its reference image shows only the extended bright galaxy. In this case, the reference image is helpful and the RMS image is acceptable since the variability is centred on the source. Of the sources passing visual inspection, only 39 (15 per cent) have well-centred RMS image sources.

4.5 Light curves from nearby pixels

For the objects that passed the RMS check, we performed a two-step final confirmation. We used another TESS light curve pipeline (Vallely et al. 2021) to verify the presence of variability and constructed a 5 × 5 pixel grid of light curves centred on the source pixel of each object (Figs 7−13). These grids allowed for a final contamination check. In particular, we were confident in a signal if the neighbouring pixels had the same features as the central light curve but at lower amplitudes, with an expected fall-off consistent with the PRF (e.g. NGC 4395, in Fig. 8). One might be concerned that the amplitude at the position of ESO 252–018A (Fig. 11), for example, is slightly lower than in an adjacent pixel. However, the centring inconsistency is likely an issue with coordinates rather than the source of variability. In this step, we reject 10 of the 39 sources that passed the RMS check.

4.6 Final candidates

The final 29 AGN candidates are presented in Tables 4 and 5 summarizes the outcomes for each source in the original HyperLEDA and GLADE samples. Based on the RMS images and light-curve grids, we assign each final candidate one of the three confidence levels. High-confidence sources show no instrumental issues or stellar contamination. They also have similar, lower amplitude trends in the nearby pixels. In Figs 7−11, we show the light curve grids for our five high-confidence sources. Medium-confidence sources

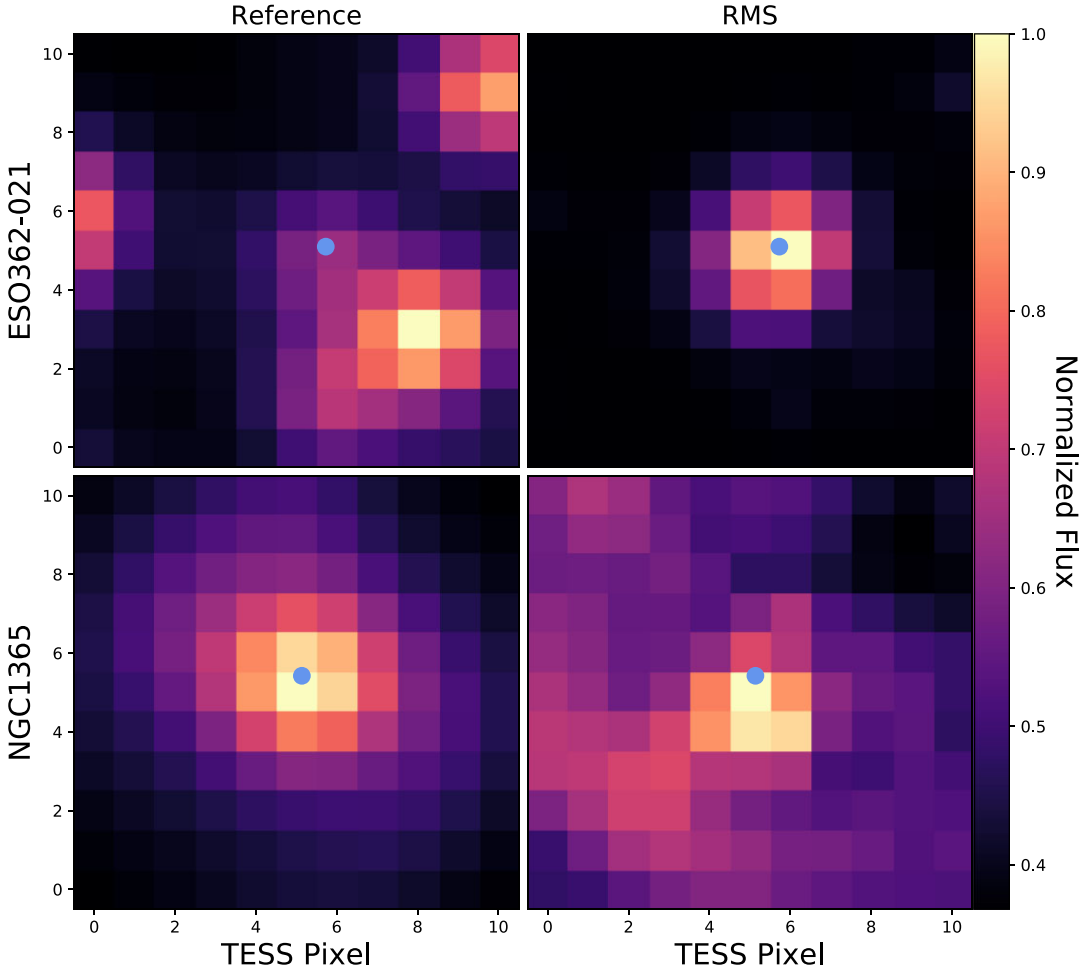

Figure 6. Reference (left-hand panel) and RMS images (right-hand panel) of ESO 362–021 (top panel) and NGC 1365 (bottom panel), normalized to the brightest pixel. Each pixel covers 21 arcsec on the sky. The centre of the galaxy is at the blue dot. ESO 362–021 is faint relative to nearby stars, but the RMS image shows that it is the variable source. On the other hand, NGC 1365 is bright but its RMS image has some additional structure and thus calls for further confirmation.

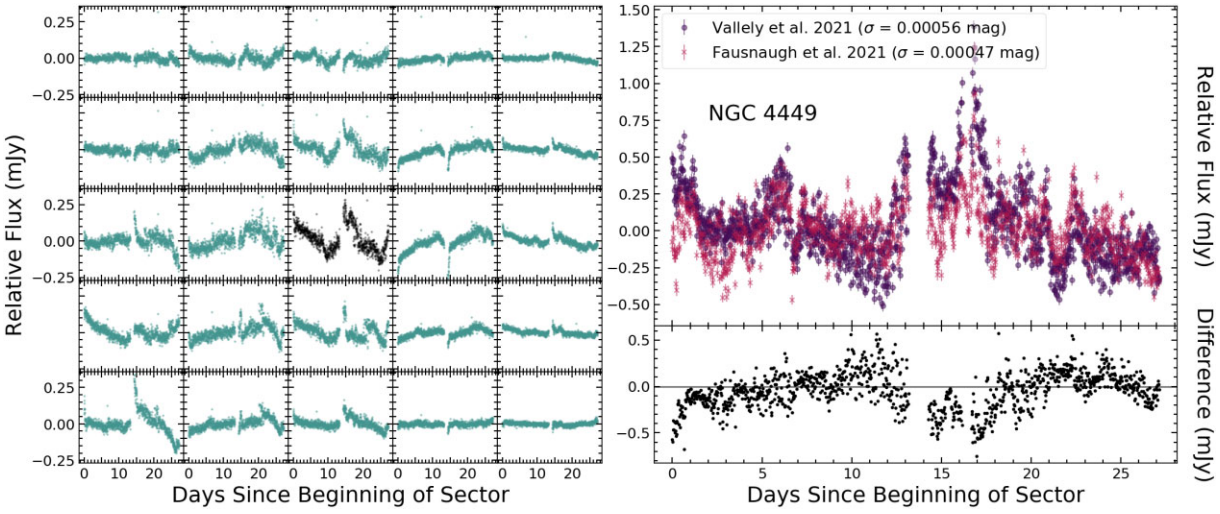

Figure 7. Final confirmation step for the low-mass, high-confidence source NGC 4449. The grid of Sector 22 light curves (left-hand panel) is for the source's central and neighbouring pixels using the Vallely et al. (2021) pipeline. The corresponding PSF photometry version is shown with pink x's (top right-hand panel), with the original reduction used in the visual inspection shown in purple and the difference between the two in the bottom right-hand panel.

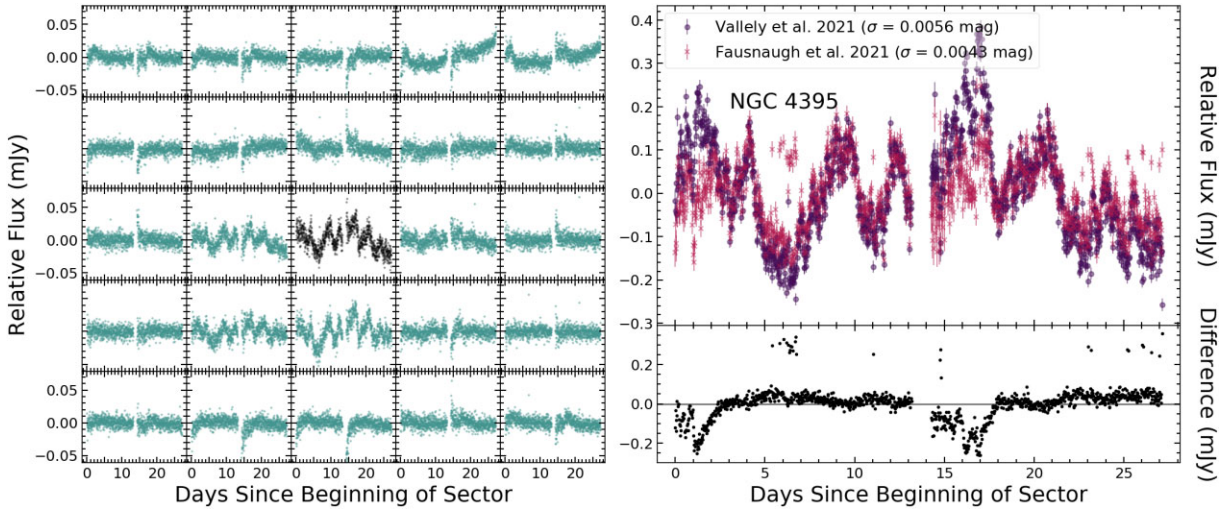

Figure 8. Same as Fig. 7, but for high-confidence candidate NGC 4395.

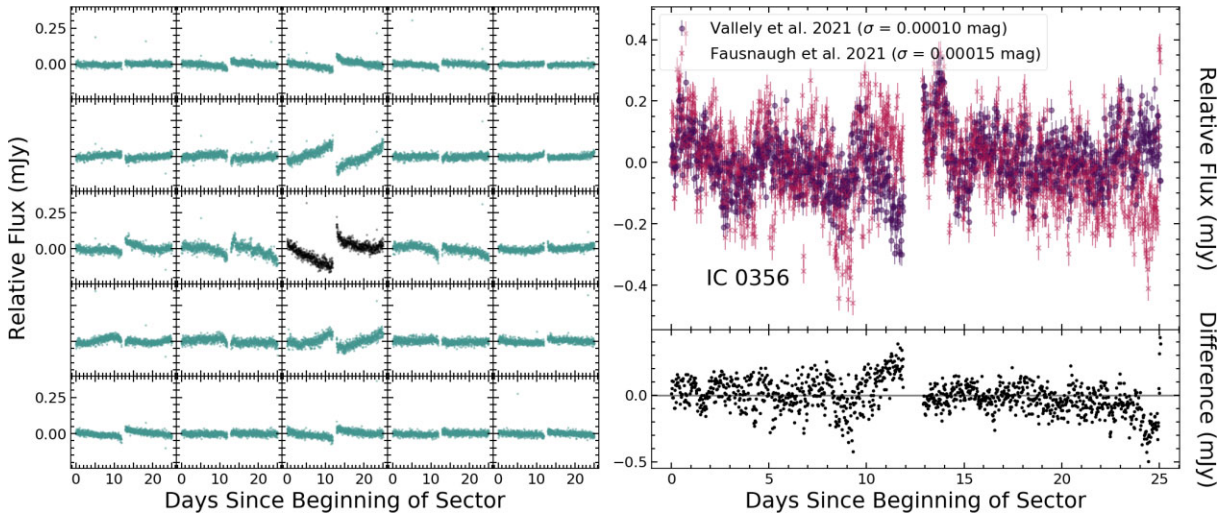

Figure 9. Same as Fig. 7, but for high-confidence candidate IC 0356 in Sector 19. The discontinuity at the time of a data downlink in the pixel grid light curves is fairly typical.

show some evidence of systematic problems or nearby stars, but likely not enough to explain the observed variability. We show light curve grids for two medium-confidence sources in Fig. 12. Low-confidence sources may be AGNs, but there are enough indications of systematic errors or contamination to potentially explain the observed variability. In Fig. 13, we show representative examples of low-confidence sources. In total, there are 5 high-confidence sources, 7 medium-confidence sources, and 17 low-confidence sources.

Because we started with rough BH mass estimates, we attempted to re-estimate M_{BH} for each of the final AGN candidates. First, we searched the literature for black hole mass estimates and found 18 estimates. Most sources only had one literature estimate, but for those with more, we chose estimates in the order (1) spatially resolved kinematics, (2) virial mass using broad lines, and (3) stellar velocity dispersion. These preferred mass estimates are included in Table 4. Secondly, we found morphology classifications for the candidates using the NASA Extragalactic Database (NED).[6] For the HyperLEDA and GLADE subsamples, we originally took the M_{BH} upper limits using the Graham (2007) relation. By incorporating the galaxy morphologies, we scaled down the absolute *K*-band measurements to bulge magnitudes using the median scaling factors found for each type in Graham & Worley (2008). Thirdly, using NED and the Extragalactic Distance Database (Tully et al. 2009), we found redshift-independent distances for 23 of the candidates. We gave preference to the distances in the order: (1) the Cepheid period–luminosity relation, (2) tip of the red-giant branch (TRGB), (3) supernovae Ia, (4) the Tully–Fisher relation, and (5) surface brightness fluctuations. For the six candidates without redshift-independent

[6]The NASA/IPAC Extragalactic Database (NED) is operated by the Jet Propulsion Laboratory, California Institute of Technology, under contract with the National Aeronautics and Space Administration.

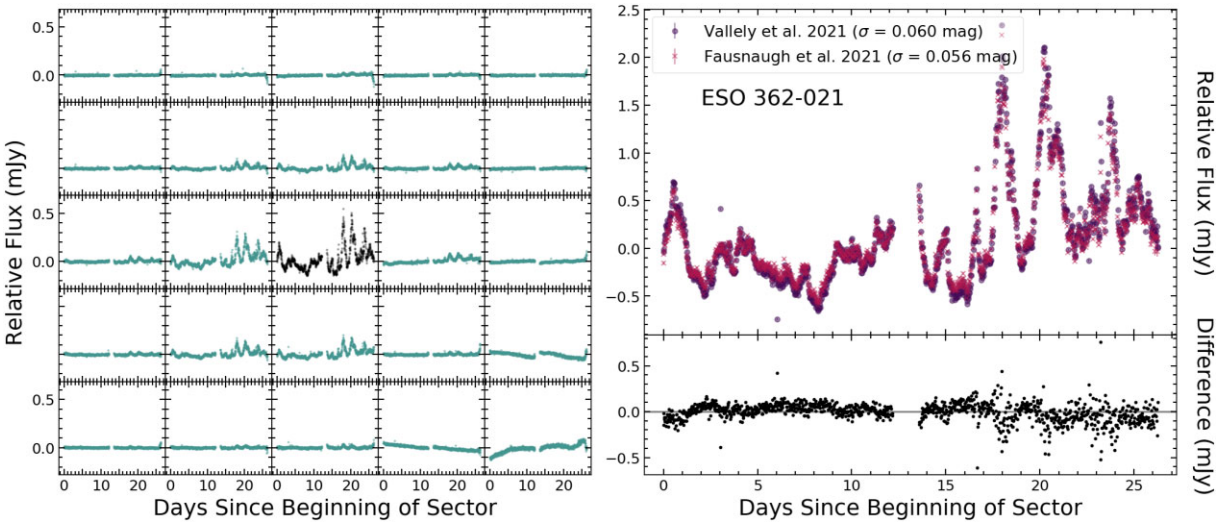

Figure 10. Same as Fig. 7, but for high-confidence candidate ESO 362–021 in Sector 5. This source corresponds to the outlier at high variability in Fig. 4.1 and is a known blazar.

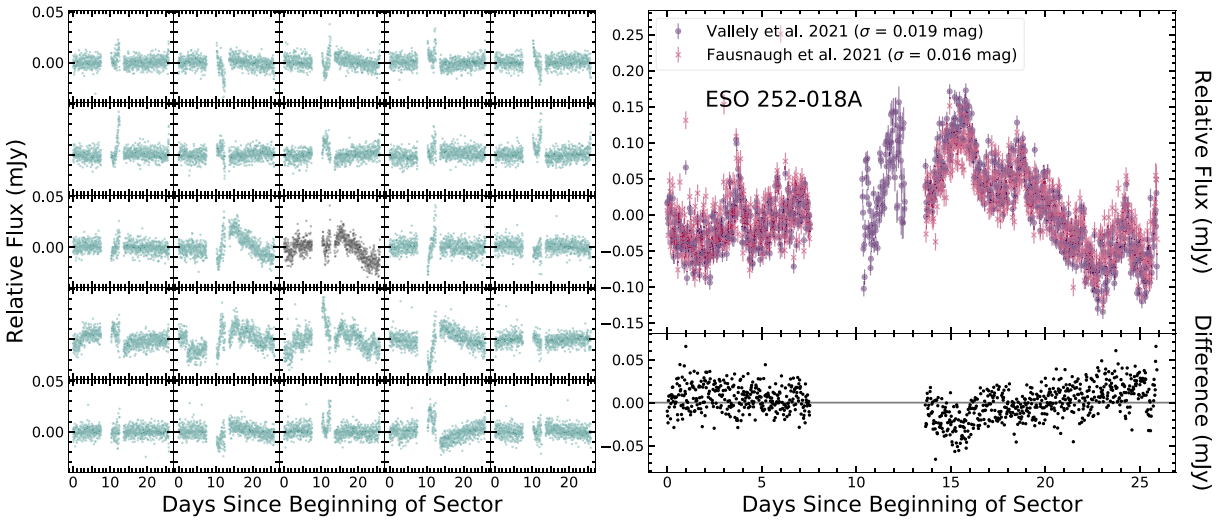

Figure 11. Same as Fig. 7, but for high-confidence candidate ESO 252–018A in Sector 4. The stricter rejection procedure in the reduction methods outlined in Fausnaugh et al. (2021) yielded a different temporal range for this light curve and a few others.

distance, we used their spectroscopic redshifts to estimate luminosity distances. For the remainder of this work, we use the literature M_{BH} where available, and otherwise employ our re-estimated *K*-band values.

5 CLASSIFYING CANDIDATES USING OTHER AGN DIAGNOSTICS

In this section, we compare our TESS variability selection to other methods of AGN selection. In Section 5.1, we describe our investigation of the source outcomes of all the galaxies in the HyperLEDA sample that are labelled as AGNs. We then used archival and new data to identify which objects can be selected as AGNs using other methods, including line diagnostics (Section 5.2), colour–colour diagrams (Section 5.4), and X-ray luminosity (Section 5.3). Table 4 includes the results of this search.

If a source is not found to be an AGN using methods other than variability, that does not rule out the possibility of it being an AGN. In Yuk et al. (2022), emission-line diagnostic diagrams classify ∼30 per cent of variability-selected AGN candidates as star forming. For low-mass AGNs, spectroscopic selection misses 75 per cent of variability-selected candidates in Baldassare et al. (2020) and 81 per cent in Ward et al. (2022).

5.1 AGNs in HyperLEDA not selected with variability

HyperLEDA includes nuclear activity classifications primarily taken from Véron-Cetty & Véron (2006). Among the sources that passed the stellar contamination check, 231 are catalogued as AGNs, and 57 are selected for visual inspection (Section 5) using the brightness or variability cut (Section 4.3). Following visual inspection, six of these AGNs remain. The six objects are in our final candidate list,

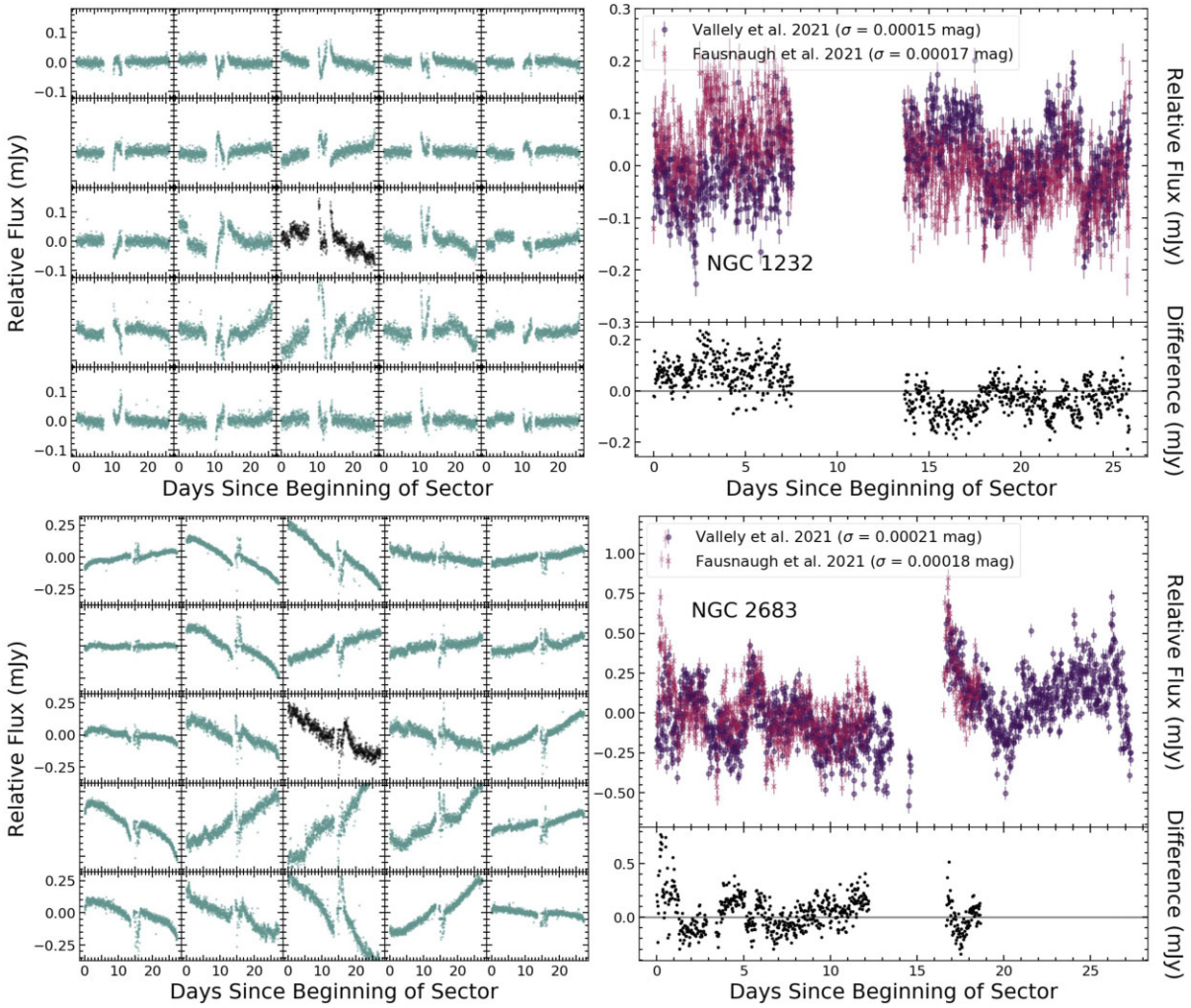

Figure 12. Same as Fig. 7, but for representative medium-confidence candidates. For each source, there is decent agreement between the two reductions. Top panel: Sector 4 light curves of NGC 1232. The short-term variations are strongest in the centre of the grid, and there is an expected decrease in amplitude in the neighbouring light curves. Bottom panel: Sector 21 light curves of NGC 2683. The light curves from the neighbouring pixels have significant long-term trends, which are likely systematics, but the short-term signal from the central pixel is present in an expected way in the neighbouring light curves.

so 11 per cent of known AGNs that are sufficiently bright or variable for visual inspection became final AGN candidates. Thus, just as variability selection using TESS uncovers new AGNs, other methods select many AGNs inaccessible to TESS. Likely contributing to this discrepancy are obscuration, stellar contamination, and intrinsically low levels of variability.

5.2 Emission-line diagnostic diagrams

The BPT/VO87 diagrams (Baldwin et al. 1981; Veilleux & Osterbrock 1987; Kewley et al. 2006) are common methods for distinguishing between AGNs and galaxies with star formation. We examined $\log([\mathrm{O\,III}]/\mathrm{H}\beta)$ versus $\log([\mathrm{N\,II}]/\mathrm{H}\alpha)$ and $\log([\mathrm{O\,III}]/\mathrm{H}\beta)$ versus $\log([\mathrm{S\,II}]/\mathrm{H}\alpha)$. The forbidden-line distinction is also used in the WHAN diagram ($\mathrm{EW}_{\mathrm{H}\alpha}$ versus $[\mathrm{N\,II}]/\mathrm{H}\alpha$, Cid Fernandes et al. 2010, 2011), which requires fewer lines and selects a higher proportion of galaxies as AGNs.

We used NED to obtain optical spectra from the Sloan Digital Sky Survey (SDSS Blanton et al. 2017), 6dF (Jones et al. 2009), the Palomar Double Spectrograph (Oke & Gunn 1982), the Boller & Chivens Spectrograph on the 2.3-m Bok Telescope,[7] and the Intensified Image Dissector Scanner on the Kitt Peak 2.1-m telescope (Goad 1979). We also searched for spectra using the Gemini Observatory, NOIRLab, European Southern Observatory, Keck, and Las Cumbres Observatory (Brown et al. 2013) archives. Additionally, we obtained two spectra using the Low Dispersion Survey Spectrograph 3[8] (LDSS3) on the Magellan Clay telescope at Las Campanas Observatory and two with the Supernova Integrated Field Spectrograph (SNIFS; Lantz et al. 2004) on the University of Hawai'i 88-inch telescope as part of the Spectral Classification of Astronomical Transients (SCAT; Tucker et al. 2018, 2022) survey.

In total, we found or acquired spectra for 21 of the 29 candidates. Table 4 includes the origin of each spectrum. Using penalized pixel-fitting (`PPXF`; Cappellari & Emsellem 2004; Cappellari 2017), we were able to fit all the necessary lines for 15 spectra and all the lines besides Hβ for three objects. When fitting emission line

[7] http://james.as.arizona.edu/~psmith/90inch/bcman/html/bcman.html
[8] http://www.lco.cl/technical-documentation/index-2/

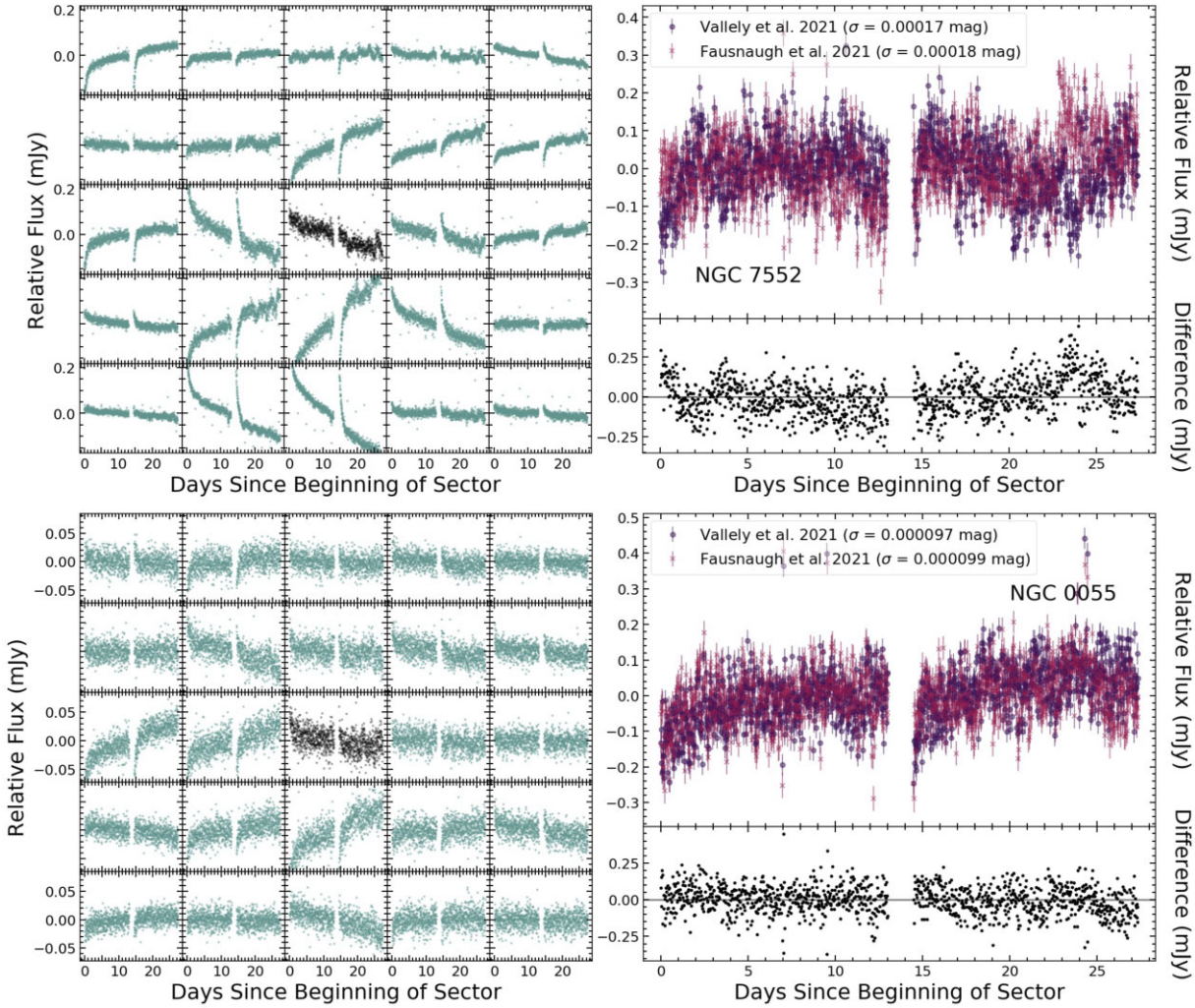

Figure 13. Same as Fig. 7, but for representative low-confidence candidates. Top panel: The pixels surrounding the Sector 2 light curve of NGC 7552 show similar behaviour to those of NGC 2683 (Fig. 12). NGC 7552 is lower confidence, primarily because of the decreased detectability of similar, but lower amplitude, variability in the neighbouring light curves. Bottom panel: The Sector 2 light curves of NGC 0055 show a weak signal, leading to its designation as low confidence.

strengths, PPXF accounts for stellar absorption by drawing on its large library of stellar population templates. This approach allows for proper measurement of weak emission lines. For two candidates with unconstrained lines using PPXF, we used the SDSS line fits (Brinchmann et al. 2004). Thus, 17 objects are in all three emission-line diagnostic diagrams shown in Fig. 14 but the WHAN diagram includes 20 candidates. In these diagrams, we distinguish candidates of different confidences with different markers.

Of the 17 variability-selected AGN candidates for which we could use all three emission-line diagnostic diagrams, 13 (76 per cent) are selected as AGNs by at least one of the diagrams, but none are selected by all three. In addition, the LDSS3 spectrum of ESO 362–021 and the SNIFS spectrum of ESO 605–016 had unconstrained line fits but clearly exhibit broad lines. In total, we note the presence of broad emission lines in five of the 21 AGN candidates with spectra. This feature shows that at least these five sources are unobscured AGNs. Table 6 summarizes these spectroscopic characterizations. These results demonstrate the strength of our methodology in two ways. First, the selection percentage is significantly higher than the overall AGN fraction (∼25 per cent, Kewley et al. 2006), further confirming the physicality of the detections. Second, the emission-line diagnostic methods do not select some of our candidates, thus corroborating that variability selection provides a complementary sub-population of AGNs.

5.3 X-ray detections

If the X-ray luminosity originating from a galaxy exceeds the expected contribution from X-ray binaries, the galaxy must host an AGN (e.g. Elvis et al. 1978). We queried the individual catalogues included in the results of a HEASARC Master X-ray Catalog[9] search: ASCAGIS (Ueda et al. 2001, 2005), BMWCHANCAT (Romano et al. 2008), BMWHRICAT (Panzera et al. 2003), CHAMPPSC (Kim et al. 2007), CXOXASSIST (Ptak & Griffiths 2003), EINGALCAT (Fabbiano, Kim & Trinchieri 1992), RASS2RXS (Boller et al. 2016), RASS6DFGS (Mahony et al. 2010), RASSBSCPGC (Zimmermann et al. 2001), TARTARUS (Turner et al. 2001), WGACAT (White,

[9]https://heasarc.gsfc.nasa.gov/W3Browse/all/xray.html

Table 4. AGN candidates.

Name	RA	Dec.	Conf.	Est. $\log(M_{BH}/M_\odot)$	Lit. $\log(M_{BH}/M_\odot)$	Ref	Lit. AGN	Ref	$\log(z)$	Dist.	Ref	Morph.	I	σ	$\log(L_X/erg\,s^{-1})$	W1−W2	W3−W4	Spec.	Broad Lines	$\log([O\,III]/H\beta)$	$\log([N\,II]/H\alpha)$	$\log([S\,II]/H\alpha)$	Hα Emission EW
	(°)	(°)								Mpc			Vega mag	Vega mag		Vega mag	Vega mag						Å
IC 0356	61.945	69.812	High	8.2	7.7	1	–	–	−2.53	22 ± 4	21	Sb	8.7	0.00015	40.6	0.02 ± 0.03	1.31 ± 0.05	PDS	N	−0.6 ± 0.3	0.07 ± 0.03	−0.49 ± 0.08	2.4 ± 0.1
ESO 252–018A	79.957	−45.779	High	7.7	7.5	2	Sy 2	10	−1.46	154	z	S0	14.6	0.016	42.6	0.96 ± 0.03	2.27 ± 0.03	–	–	–	–	–	–
ESO 362–021	80.742	−36.459	High	8.3	–	–	Sy 1	11	−1.25	253	z	E/S0	13.5	0.056	43.9	0.98 ± 0.03	2.26 ± 0.02	LDSS3	Y	–	–	–	–
NGC 4395	186.454	33.547	High	4.3	5.5	3	Sy 1	13	−2.97	4.3 ± 0.4	22	Sm	12.8	0.0043	39.3	0.79 ± 0.03	3.09 ± 0.04	SDSS	Y	0.99 ± 0.01	−0.71 ± 0.01	−0.45 ± 0.01	68.2 ± 0.6
NGC 4449	187.046	44.094	High	5.6	3.9	4	–	–	−3.16	4.3 ± 0.4	23	Sm	9.6	0.00047	38.2	0.16 ± 0.03	3.64 ± 0.03	IIDS	N	0.5 ± 0.0	−0.90 ± 0.02	−0.86 ± 0.02	27.3 ± 0.1
NGC 1232	47.439	−20.579	Med.	7.5	6.6	5	–	–	−2.27	26 ± 4	21	SABc	9.3	0.00017	38.7	−0.05 ± 0.03	2.3 ± 0.2	6dF	N	–	0.42 ± 0.15	0.15 ± 0.22	0.5 ± 0.1
ESO 254–017	91.649	−47.499	Med.	8.7	–	–	Sy 2	12	−1.53	131	z	E	11.9	0.0022	43.0	0.21 ± 0.03	1.96 ± 0.06	LDSS3	Y	0.2 ± 0.1	0.27 ± 0.04	−0.29 ± 0.09	2.8 ± 0.2
NGC 2654	132.299	60.221	Med.	7.7	7.7	–	–	–	−2.35	32 ± 4	24	SBab	11.3	0.00078	–	−0.03 ± 0.03	1.39 ± 0.08	SDSS	N	0.47 ± 0.08	0.26 ± 0.04	−0.011 ± 0.051	0.71 ± 0.05
NGC 2683	133.173	33.422	Med.	7.5	7.4	4	LINER	14	−2.86	9.4 ± 0.3	25	Sb	8.6	0.00018	39.0	0.09 ± 0.03	1.55 ± 0.04	PDS	N	0.28 ± 0.05	0.21 ± 0.02	0.022 ± 0.026	2.6 ± 0.1
UGC 04767	136.439	36.355	Med.	8.1	–	–	–	–	−1.62	106	z	S0	12.5	0.0029	–	−0.08 ± 0.03	1.8 ± 0.1	SDSS	N	−0.008 ± 0.254	−0.036 ± 0.102	−1.0 ± 0.6	0.57 ± 0.09
NGC 2759	137.155	37.622	Med.	8.1	–	–	–	–	−1.64	103 ± 19	26	E-S0	12.4	0.0020	–	−0.06 ± 0.03	1.2 ± 0.5	SDSS	N	0.027 ± 0.090	0.032 ± 0.072	−1.0 ± 0.6	0.63 ± 0.07
NGC 2782	138.521	40.114	Med.	7.8	8.0	4	Sy 2	15	−2.07	37 ± 14	27	SABa	10.9	0.00067	39.9	0.48 ± 0.03	2.72 ± 0.02	Bok	N	0.083 ± 0.010	−0.24 ± 0.01	−0.42 ± 0.01	21.0 ± 0.1
ESO 536–014	354.760	−25.670	Low	7.9	–	–	–	–	−1.50	142 ± 31	28	Sb	12.6	0.0022	–	−0.06 ± 0.03	2.1 ± 0.1	6dF	N	0.27 ± 0.29	0.007 ± 0.105	−0.68 ± 0.47	1.8 ± 0.3
NGC 0055	3.723	−39.197	Low	5.3	–	–	–	–	−3.36	1.86 ± 0.08	29	Sm	8.7	0.000099	37.5	0.08 ± 0.04	3.57 ± 0.04	–	–	–	–	–	–
NGC 0157	8.695	−8.396	Low	7.2	7.7	5	LINER	16	−2.26	12 ± 2	24	SABb	9.5	0.00025	–	0.03 ± 0.03	2.59 ± 0.03	–	–	–	–	–	–
PGC 089900	22.199	−54.357	Low	8.3	–	–	Sy 1	17	−1.03	426	z	S	14.4	0.013	44.6	1.06 ± 0.03	2.87 ± 0.03	–	–	–	–	–	–
NGC 0720	28.252	−13.739	Low	8.6	7.7	6	–	–	−2.24	26 ± 3	24	E	9.3	0.00031	39.2	−0.03 ± 0.03	1.12 ± 0.08	–	–	–	–	–	–
NGC 0959	38.100	35.495	Low	5.4	5.5	4	–	–	−2.70	11 ± 2	24	Sm	11.6	0.0011	–	0.01 ± 0.04	2.91 ± 0.06	Bok	N	0.22 ± 0.02	−0.56 ± 0.02	−0.35 ± 0.01	6.91 ± 0.07
NGC 0991	38.886	−7.154	Low	6.0	–	–	–	–	−2.29	19 ± 4	27	SABc	12.1	0.0018	39.2	−0.04 ± 0.04	2.5 ± 0.2	SDSS	N	0.3 ± 0.1	0.041 ± 0.044	0.04 ± 0.04	1.08 ± 0.07
UGC 02509	45.850	4.492	Low	7.3	–	–	–	–	−1.70	79 ± 15	24	Sbc	13.3	0.010	–	0.12 ± 0.03	1.99 ± 0.05	SNIFS	N	–	−0.20 ± 0.07	−0.58 ± 0.15	1.7 ± 0.1
NGC 1332	51.572	−21.335	Low	8.0	8.8	7	–	–	−2.27	25 ± 3	24	E-S0	9.1	0.00046	39.3	−0.03 ± 0.03	1.22 ± 0.05	–	–	–	–	–	–
NGC 1365	53.402	−36.141	Low	8.0	6.0	5	CLAGN	18	−2.26	18.3 ± 0.5	30	Sb	8.4	0.00017	40.2	0.76 ± 0.03	3.41 ± 0.02	6dF	Y	0.23 ± 0.01	−0.28 ± 0.01	−1.04 ± 0.02	34.5 ± 0.2
NGC 1398	54.717	−26.338	Low	8.3	8.0	8	–	–	−2.33	29 ± 6	24	SBab	8.4	0.00021	40.6	0.01 ± 0.03	1.20 ± 0.08	–	–	–	–	–	–
NGC 2146	94.657	78.357	Low	7.7	7.3	4	AGN	19	−2.53	17 ± 3	27	SBab	9.6	0.00019	39.4	0.60 ± 0.03	2.97 ± 0.02	Bok	N	−0.23 ± 0.02	−0.23 ± 0.01	−0.55 ± 0.01	15.70 ± 0.05
NGC 2976	146.815	67.916	Low	5.9	5.1	4	–	–	−5.00	3.6 ± 0.1	31	Sc	9.2	0.00015	38.6	0.04 ± 0.03	2.88 ± 0.04	SDSS	N	0.13 ± 0.01	−0.52 ± 0.01	−0.69 ± 0.01	73.1 ± 0.6
NGC 3183	155.454	74.177	Low	7.3	–	–	–	–	−1.99	37 ± 7	24	SBbc	11.0	0.00051	–	0.27 ± 0.03	2.17 ± 0.03	–	–	–	–	–	–
NGC 4244	184.374	37.807	Low	5.7	5.7	9	–	–	−3.09	4.4 ± 0.2	32	Scd	10.9	0.00041	37.0	−0.04 ± 0.03	2.22 ± 0.12	SDSS	N	−0.18 ± 0.13	−0.47 ± 0.04	−0.23 ± 0.04	3.0 ± 0.1
NGC 7552	349.045	−42.584	Low	7.7	7.3	5	LINER	20	−2.27	20 ± 4	27	Sab	9.3	0.00018	40.8	0.79 ± 0.03	3.12 ± 0.02	6dF	N	−0.65 ± 0.04	−0.12 ± 0.01	−0.66 ± 0.03	16.6 ± 0.1
ESO 605–016	354.279	−20.463	Low	7.8	–	–	–	–	−1.58	115	z	Sc	11.7	0.00097	–	−0.11 ± 0.03	2.3 ± 0.3	SNIFS	Y	–	−0.16 ± 0.03	−0.73 ± 0.07	1.5 ± 0.1

Note. Final candidates: For candidates originating from GLADE, we identified NGC names using NED. The references for literature M_{BH} are as follows: (1) is Richings, Uttley & Körding (2011), (2) is Lewis & Eracleous (2006), (3) is den Brok et al. (2015), (4) is Williams et al. (2021), (5) is Davis et al. (2014), (6) is Mutlu-Pakdil, Seigar & Davis (2016), (7) is Barth et al. (2016), (8) is Saglia et al. (2016), and (9) is De Lorenzi et al. (2013). The literature mass estimates generally employ higher accuracy methods than our own. However, the Williams et al. (2021) value of $\log(M_{BH}/M_\odot) = 3.91 \pm 0.81$ for NGC 4449 has significant uncertainty, and uses an extrapolation of the M–σ of Tremaine et al. (2002). In this case, our $\log(M_{BH}/M_\odot)$ estimate of 5.6 may be more representative. The references for sources selected as AGNs in the literature are as follows: (10) is Glass (1981), (11) is Westerlund & Stokes (1966) and Danziger et al. (1979), (12) is Pietsch et al. (1998), (13) is Filippenko & Sargent (1989), (14) is Spinoglio & Malkan (1989), (15) is Véron-Cetty & Véron (2006), (16) is Pulatova et al. (2015), (17) is Maza et al. (1994), (18) is Risaliti, Maiolino & Bassani (2000) and Matt, Guainazzi & Maiolino (2003), (19) is Tzanavaris & Georgantopoulos (2007) and Ruschel-Dutra et al. (2017), and (20) is Dudik et al. (2007). The distance references are as follows: (21) is Tully et al. (2008), (22) is Thim et al. (2004), (23) is Jacobs et al. (2009), (24) is Tully, Courtois & Sorce (2016), (25) is Karachentsev et al. (2015), (26) is Theureau et al. (2007), (27) is Tully & Fisher (1988), (28) is Kourkchi et al. (2020), (29) is Bhardwaj et al. (2016), (30) is Riess et al. (2016), (31) is Tully et al. (2013), and (32) is Radburn-Smith et al. (2011). Distance references marked as 'z' are converted from the given redshifts using the cosmological parameters adopted by HyperLEDA: $H_0 = 70\,km\,s^{-1}\,Mpc^{-1}$, $\Omega_M = 0.27$, and $\Omega_\Lambda = 0.73$. For these conversions, we used Wright (2006). We took available galaxy morphologies from HyperLEDA. Morphologies for ESO 362–021 and PGC 089 900 were estimated using DSS images. For candidates from the GLADE subsample, we identified morphologies in de Vaucouleurs et al. (1991). When possible, we used the I magnitudes catalogued in HyperLEDA. However, for NGC 4395 and NGC 0055, we estimated I using the J mag measurements catalogued in GLADE (Section 2), and the NGC 0959 value is from Heraudeau & Simien (1996). Estimated X-ray luminosity (see Section 5.3) is in the 0.5–10-keV band. The 'Spec.' column provides the name of the telescope and/or spectrograph used for the emission-line diagnostic diagrams (Fig. 14). We use LDSS3 to designate the Low Dispersion Survey Spectrograph 3 on the Magellan Clay telescope, IIDS for the Intensified Image Dissector Scanner on the Kitt Peak 2.1-m telescope, PDS to refer to the Palomar Double Spectrograph, and Bok for the Boller & Chivens Spectrograph on the 2.3-m Bok Telescope.

Table 5. Source outcomes for entire sample.

Name	RA (°)	Dec. (°)	Source outcome
PGC 124374	0.001	−41.423	Low variability
PGC 520795	0.001	−45.954	Low variability
PGC 143101	0.003	−59.013	Low variability
PGC 130936	0.004	−40.903	Contaminated (REFCAT2)
00001208 + 6028060	0.050	60.468	Not AGN-like
PGC 198787	0.055	−27.633	Contaminated (ATLAS-VAR)
PGC 780808	0.102	−25.272	RMS PRF off-centre
PGC 736802	0.201	−28.838	Contaminated (ASAS-SN)
NGC 0055	3.723	−39.197	Candidate
NGC 1247	48.060	−10.481	Grid not AGN-like

Note. Names, coordinates, and the source outcome for the whole sample (HyperLEDA and GLADE). Names of GLADE sources that do not become candidates are from 2MASS. We shorten these names by excluding the prefix 2MASX J. While we include in the rows shown sources representing each of the possible outcomes, the full table is sorted by right ascension. First, sources removed due to expected stellar contamination (Section 4.2) are designated as 'contaminated' with a specification of the database of origin for the star of concern (REFCAT2, ATLAS-VAR, or ASAS-SN Variable Stars Database). A 'Source Outcome' of 'low variability' describes candidates that passed the contamination cut but have $I > 13$ mag and are not in the top 10 per cent variable at their magnitude (Fig. 3, Section 4.3). Next, 'not AGN-like' indicates that a candidate passed the variability cut but did not have AGN-like variability (Section 4.3). A final stage of 'RMS PRF off-centre' designates that a candidate has potential AGN-like variability but does not have the variable PRF in the RMS image centred on the galactic nucleus (Section 4.4). Sources with 'grid not AGN-like' have a centred PRF in the RMS image, but the grid of neighbouring light curves from the independent reduction (Section 4.5) suggested that the variability does not originate from the galaxy. Lastly, the final candidates are described by 'candidate.'

Giommi & Angelini 1994), XMMSLEWCLN (Saxton et al. 2008), XMMSSC (Webb et al. 2020), and XMMSTACK (Traulsen et al. 2020). We converted the count rates to the flux in the 0.5–10-keV band using the Portable, Interactive Multi-Mission Simulator (PIMMS, Mukai 1993). We used a power-law model with photon index 1.75 (e.g. Ricci et al. 2017) and included the Galactic absorption.[10] Where possible, we retrieved inputs for PIMMS from the catalogues or their documentation. In the absence of specified filters in the XMMSTACK and ROSAT PSPFC, we assumed the use of the medium and open filters, respectively.

Fig. 15 shows the distribution of median X-ray luminosities for the 20 candidates with catalogue matches as well as for AGNs (Seyfert, LINER, and composite galaxies) and non-AGNs detected in the eROSITA Final Equatorial Depth Survey (eFEDS, Brunner et al. 2022) field (Vulic et al. 2022). Of the 1181 HyperLEDA galaxies within 200 Mpc in the eFEDS footprint, Vulic et al. (2022) identified 94 matches, 76 of which could be classified using optical spectra. We estimated the 0.5–10-keV X-ray luminosity using the 0.5–2-keV luminosities from Vulic et al. (2022) and the conversion factor from Comparat et al. (2022).

Using the common luminosity cutoff of $L_X > 10^{42}$ erg s^{-1} (e.g. Mushotzky 2004) to exclude sources where the X-ray emission could plausibly originate from an X-ray binary population, we identify four objects (ESO 252–018A, ESO 254–017, ESO 362–021, and PGC 089900) as X-ray AGNs. However, the maximum X-ray binary contribution is lower for lower mass galaxies so a limit of 10^{39} –10^{40} erg s^{-1} is sufficient (e.g. Latimer et al. 2021) and adds three low-mass galaxies (NGC 0991, NGC 1365, and NGC 4395). Therefore, X-ray luminosity and optical variability select overlapping but different portions of AGN parameter space, as is the case with other selection methods.

[10] https://heasarc.gsfc.nasa.gov/cgi-bin/Tools/w3nh/w3nh.pl

5.4 WISE colour–colour cuts

For galaxies in which an AGN dominates the mid-IR emission, the system will be redder in mid-IR colour than stars or galaxies with weak AGNs (Assef et al. 2010; Stern et al. 2012; Assef et al. 2013). Fig. 16 shows the the Wide-Field Infrared Survey Explorer (WISE, Wright et al. 2010) W1−W2 and W3−W4 colours of the candidates. Only ESO 362–021 and ESO 252–018A are selected as AGNs using the wedge described in Assef et al. (2010, 2013). These two objects also have maximum X-ray luminosities above the selection limit described in Section 5.3. However, other studies (e.g. Stern et al. 2012) select AGNs using just a W1−W2 cutoff of 0.8 mag which adds the X-ray selected candidate PGC 089900. These results are consistent with the low fraction of MIR-selected AGNs in other studies comparing selection methods (e.g. Laurent et al. 2000).

6 DISCUSSION

We searched for strongly variable AGNs using TESS light curves of 142 061 galaxies. We selected our sample from two galaxy catalogues. First, we used HyperLEDA sources in nine TESS sectors to identify AGNs without restrictions on M_{BH}. Secondly, we considered an all-sky sample of 4366 low-mass galaxies from GLADE. Within these samples, we identify 29 optically varying AGN candidates, of which 18 are newly identified. Although the GLADE sample comprised only 3 per cent of the total sample, 17 per cent of the final AGN candidates originated from GLADE. It is unsurprising to see this over-representation of galaxies from the GLADE sample since lower mass AGNs tend to have lower time-scales of variability (e.g. Kelly et al. 2009) and therefore are more likely to be detectable using a single TESS sector.

The primary goal of our study was the identification of variable low-mass AGNs with TESS. Fig. 17 shows the distribution of estimated black hole mass for the AGN candidates. Of the 29 candidates, 8 have estimated $M_{BH} \lesssim 10^6 M_\odot$ (see Table 4). Two of the low-mass galaxies are known AGNs and three of the seven low-mass galaxies with available spectra are selected as AGNs in at least one of the emission-line diagnostic diagrams (Fig. 14). Overall, 76 per cent of the candidates with available spectra are selected as AGNs in at least one line ratio diagram. In this percentage, we include composite and LINER galaxies because they likely include the contribution of some AGN light (e.g. Kewley et al. 2006).

We independently selected NGC 4395 as the strongest low-mass candidate, corroborating the Burke et al. (2020) identification of its TESS variability. NGC 4395 is a particularly close dwarf AGN (d = 4.3 Mpc). We estimated the distance limit at which the variability of NGC 4395 would be detectable by TESS. Using Fig. 3, we found that NGC 4395 would be dominated by noise if it were one magnitude fainter. This corresponds to sources ∼1.4 times more distant and thus the distance probed by TESS for comparable levels of variability to NGC 4395 is ∼6 Mpc. A few of our low-mass AGN candidates are more distant than 10 Mpc, but they are all more luminous than NGC 4395.

Most of our candidates are higher mass AGNs catalogued in HyperLEDA. These objects demonstrated that single TESS sectors can be sufficient for the identification of variability in AGNs with

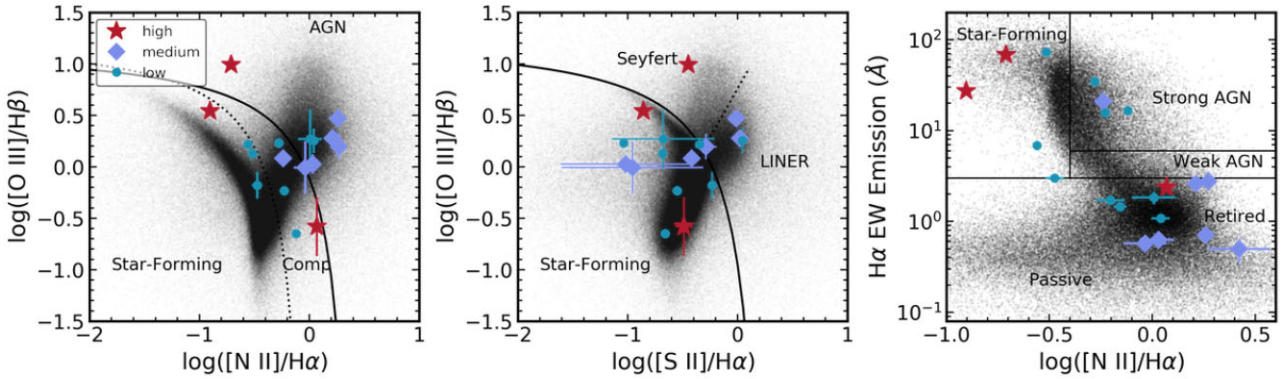

Figure 14. Emission-line diagnostic diagrams for the AGN candidates, demonstrating that variability selection allows for the identification of AGNs missed by other methods. The high-confidence candidates are shown by red stars, the medium-confidence by purple diamonds, and the low-confidence by blue circles. The black points are galaxies with spectra in SDSS Data Release 8 (Eisenstein et al. 2011). Left-hand panel: log([O III]/Hβ) versus log([N II]/Hα), which is one of the BPT/VO87 diagrams (Baldwin et al. 1981; Veilleux & Osterbrock 1987). The solid curve was theoretically determined in Kewley et al. (2001) to separate star-forming regions and AGN. The dotted curve follows the empirical separation from Kauffmann et al. (2003). Center panel: log([O III]/Hβ) versus log([S II]/Hα) (Baldwin et al. 1981; Veilleux & Osterbrock 1987). The solid curve originates from Kewley et al. (2001), while the dotted line theoretically differentiating between Seyferts and LINERs comes from Kewley et al. (2006). Right-hand panel: Hα EW versus log([N II]/Hα) diagram (WHAN, Cid Fernandes et al. 2011). Of the 17 candidates present in all three diagrams, 76 per cent are selected as AGNs by at least one of these metrics, but none are selected by all three. Table 6 provides more specific percentages by diagram.

Table 6. AGN candidate selection in emission-line diagnostic diagrams (Fig. 14).

[O III]/Hβ versus [N II]/Hα			
AGN	1 (5.9 %)	LINER	7 (41.1 %)
Composite	5 (29.4 %)	Star forming	4 (23.5 %)
[O III]/Hβ versus [S II]/Hα			
Seyfert	1 (5.9 %)	LINER	4 (23.5 %)
Star forming	12 (70.6 %)		
$EW_{H\alpha}$ versus [N II]/Hα			
Strong AGN	4 (20.0 %)	Weak AGN	0 (0.0 %)
Passive or retired	12 (60.0 %)	Star forming	4 (20.0 %)

Note. There are 17 objects in the [O III]/Hβ versus [N II]/Hα and [O III]/Hβ versus [S II]/Hα diagrams, and 20 objects in the $EW_{H\alpha}$ versus [N II]/Hα (WHAN) plot.

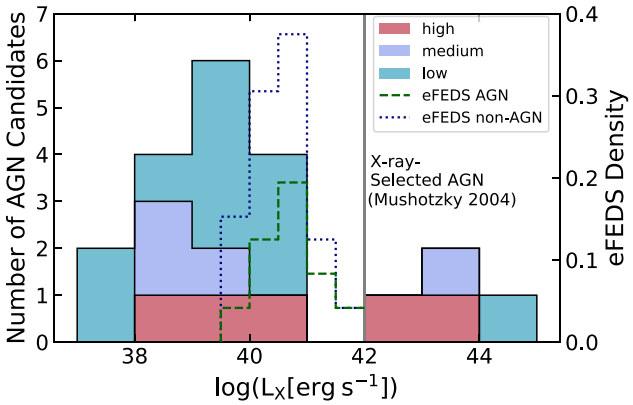

Figure 15. The filled stacked histograms show the median X-ray luminosity for the 20 detected AGN candidates by confidence level. All five of our high-confidence candidates have X-ray detections. The X-ray luminosity cutoff from Mushotzky (2004) marks the value at which the source of the emission must be an AGN rather than star formation. This cutoff yields four X-ray selected AGN, while the Latimer et al. (2021) criterion for low-mass galaxies selects three additional sources. The unfilled stacked histogram shows the X-ray luminosity distribution for HyperLEDA galaxies within 200 Mpc detected in the eROSITA Final Equatorial Depth Survey (eFEDS), with the AGN and non-AGN populations separated with emission-line diagnostic diagrams (Vulic et al. 2022).

estimated black hole masses up to $\sim 10^9$ M$_\odot$. For GLADE objects, we generated light curves for any relevant primary mission sector, whereas the HyperLEDA light curves originate from just 9 of the 26 TESS sectors. A natural next step would be an investigation of the HyperLEDA galaxies in the remaining sectors, including the extended missions, to corroborate candidate AGNs and identify additional candidates that were not included in our sample. These sectors are also potentially useful for sources that we did not select thanks to variability amplitudes and time-scales being temporarily unobservable or because of more drastic changing-look events (e.g. Ichikawa et al. 2019; Wang et al. 2019; Lawther et al. 2023).

According to the correlation in Kelly et al. (2009), we would expect these higher masses ($\sim 10^9$ M$_\odot$) to correspond to a τ_{DRW} of $\gtrsim$500 d. However, it is possible that we selected the high-mass AGNs that fall below this relation because of their more rapid variations. This sample will enable further examination of the $\tau_{DRW}-M_{BH}$ relation, as well as of the underlying integrity of the DRW model. The damped random walk is the simplest of the continuous autoregressive moving average (CARMA Kelly et al. 2014) models. Another CARMA model, called the damped harmonic oscillator, provided a better fit than the DRW to the variability of Zw229-15 (Kasliwal, Vogeley & Richards 2017) and the parameters have potential to better map on to specifics of the accretion disc (e.g. Moreno et al. 2019; Yu et al. 2022). Especially considering the high cadence of TESS, similar model comparisons using current and future TESS AGN candidates will contribute to attempts to describe the observed variability with physical models.

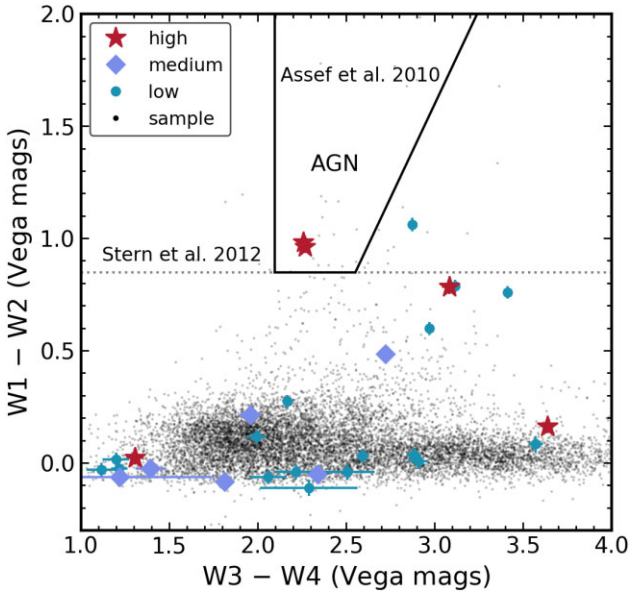

Figure 16. W1−W2 versus W3−W4 for candidate AGNs with WISE colour measurements. The high-confidence candidates are shown by red stars, the medium-confidence by purple diamonds, and the low-confidence by blue circles. In total, 10 000 random HyperLEDA sources that are at least as close as farthest AGN candidate are plotted in black. Two candidates are selected as AGNs using the wedge from Assef et al. (2010), but a third galaxy is selected using the criterion from Stern et al. (2012), which only uses W1−W2. All three are also X-ray selected (Section 5.3).

Using our methodology and assuming a constant rate of HyperLEDA AGN candidates in each TESS primary mission sector, we would roughly expect to identify 45 additional AGN candidates with similarly strong variability amplitudes, of which ∼26 will be new and ∼8 will be in low-mass galaxies.

However, methodological iterations informed by our findings may allow for a higher candidate yield. Retrospectively, RMS images should be used early on because of the extensive stellar variable contamination created by TESS's low angular resolution. Most seemingly AGN-like variability in TESS is, in fact, stellar in origin. However, 74 per cent of visually inspected candidates that passed the RMS check (Section 4.4) remained candidates following the final confirmation step of examining neighbouring light curves (Section 4.5). The RMS images are useful as an indication of both variability amplitude and position. In particular, one could use centroiding to identify sources with variability consistent with the galaxy nucleus. However, one should be careful about the potential bias against AGNs off-centred due to binary SMBHs (Komossa 2006) or dynamical kicks in low-mass galaxies (e.g. Mezcua & Domínguez Sánchez 2020; Bellovary et al. 2021). With the incorporation of this more robust contamination filtering early in the process, visual inspection becomes a minor or entirely replaceable step and a search for (quasi-)periodic AGN variability becomes feasible.

7 SUMMARY

In this paper, we searched for AGNs using optical variability selection with TESS. Our main results are as follows:

(i) We identified 29 AGN candidates. Of these candidates, 11 have literature classifications as AGNs, and 8 have $M_{BH} \lesssim 10^6 M_\odot$.

(ii) Using emission-line diagnostics, X-ray luminosity, and mid-IR colours, we demonstrated that variability is necessary for the selection of up to 38 per cent of the candidates. Included in this percentage are five of the eight candidates with $M_{BH} \lesssim 10^6 M_\odot$.

(iii) Our search for stochastic variability revealed the substantial effect of contamination from variable stars.

(iv) To mitigate the effect of stellar variability, we advocate for significant use of RMS images. Their early incorporation should allow for a more efficient process and a higher candidate yield.

Because of its high cadence and precision, TESS remains the best facility for searches of low-mass AGN activity on a large scale. Using an improved methodology that robustly removes stellar contamination and reduces systematic effects, one can leverage the full ability of TESS to study accretion and AGN behaviour of low-mass SMBHs.

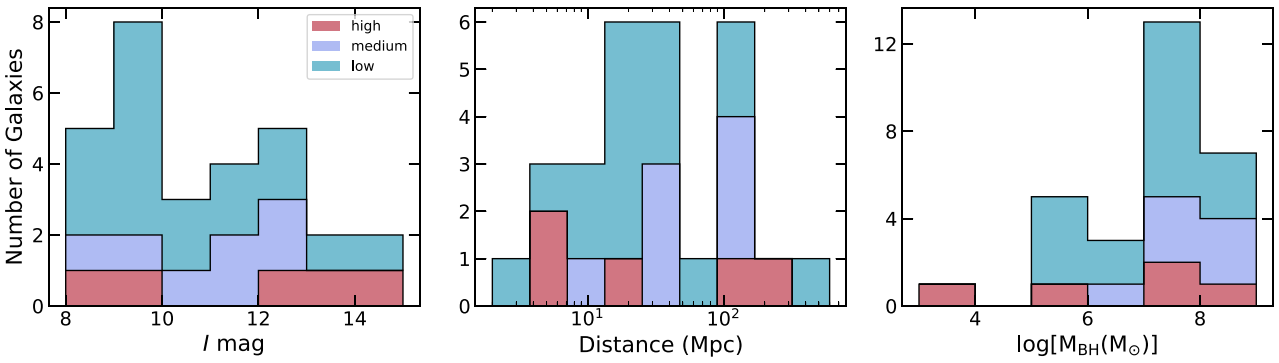

Figure 17. Histograms of apparent *I*-band magnitude, distance, and estimated black hole mass for the AGN candidates. Each histogram is stacked by candidate confidence. These histograms can be compared to those of the original sample (Fig. 2). The literature mass estimate for NGC 4449 of 3.9 ± 0.89 $M_\odot$ (Williams et al. 2021) is shown. The uncertainty is significant and the estimate requires an extrapolation of the M–σ relation from Tremaine et al. (2002). We note that our corresponding estimate is $\log(M_{BH}/M_\odot) = 5.6$ using the Graham & Worley (2008) relations and equation (14) from Graham (2007) to convert the galaxy absolute *K*-band magnitude to the spheroid absolute *K*-band magnitude, followed by the $\log(M_{BH})$.

ACKNOWLEDGEMENTS

We thank the anonymous referee for helpful suggestions that have improved the quality of this manuscript.

HT acknowledges support from Research Experience for Undergraduate program at the Institute for Astronomy, University of Hawaii-Manoa is funded through NSF grant #2050710. HT would also like to thank the Institute for Astronomy for their hospitality during the course of this project.

JTH was supported by NASA grant 80NSSC21K0136. BJS and CSK are supported by NSF grant AST-1907570/AST-1908952. BJS is also supported by NSF grants AST-1920392 and AST-1911074. CSK is also supported by NSF grant AST-181440. XD is supported by NASA grant 80NSSC22K0488.

This research has made use of the NASA/IPAC Extragalactic Database (NED), which is operated by the Jet Propulsion Laboratory, California Institute of Technology, under contract with the National Aeronautics and Space Administration.

We acknowledge the usage of the HyperLeda database (http://leda.univ-lyon1.fr).

This research has made use of data obtained from XMMSL2, the Second XMM-Newton Slew Survey Catalogue, produced by members of the XMM SOC, the EPIC consortium, and using work carried out in the context of the EXTraS project ('Exploring the X-ray Transient and variable Sky', funded from the EU's Seventh Framework Programme under grant agreement no. 607452).

DATA AVAILABILITY

This paper includes data collected by the TESS mission, which are publicly available from the Mikulski Archive for Space Telescopes (MAST). The reduced light curves for the HyperLEDA sample are available at https://github.com/mmfausnaugh/hyperleda_lc and can be downloaded following the steps explained in https://github.com/mmfausnaugh/lc_bulk/blob/main/README.md. The final candidate light curves are included in a table in the ancillary files. Other data underlying this article will be shared on reasonable request to the corresponding author.

REFERENCES

Alard C., 2000, A&AS, 144, 363
Alard C., Lupton R. H., 1998, ApJ, 503, 325
Assef R. J. et al., 2010, ApJ, 713, 970
Assef R. J. et al., 2013, ApJ, 772, 26
Auge C. et al., 2020, AJ, 160, 18
Baade W., Minkowski R., 1954, ApJ, 119, 215
Baldassare V. F., Geha M., Greene J., 2020, ApJ, 896, 10
Baldwin J. A., Phillips M. M., Terlevich R., 1981, Publ. Astron. Soc. Pac., 93, 5
Barth A. J., Boizelle B. D., Darling J., Baker A. J., Buote D. A., Ho L. C., Walsh J. L., 2016, ApJ, 822, L28
Bellovary J. M. et al., 2021, MNRAS, 505, 5129
Bhardwaj A., Kanbur S. M., Macri L. M., Singh H. P., Ngeow C.-C., Wagner-Kaiser R., Sarajedini A., 2016, AJ, 151, 88
Bilicki M., Jarrett T. H., Peacock J. A., Cluver M. E., Steward L., 2014, ApJS, 210, 9
Blanton M. R., Roweis S., 2007, AJ, 133, 734
Blanton M. R. et al., 2017, AJ, 154, 28
Boller T., Freyberg M. J., Trümper J., Haberl F., Voges W., Nandra K., 2016, A&A, 588, A103
Brinchmann J., Charlot S., Heckman T. M., Kauffmann G., Tremonti C., White S. D. M., 2004, preprint (arXiv:astro-ph/0406220)
Brown T. M. et al., 2013, Publ. Astron. Soc. Pac., 125, 1031
Brunner H. et al., 2022, A&A, 661, A1
Burke C. J., Shen Y., Chen Y.-C., Scaringi S., Faucher-Giguere C.-A., Liu X., Yang Q., 2020, ApJ, 899, 136
Burke C. J. et al., 2021, Science, 373, 789
Burke C. J., Shen Y., Liu X., Natarajan P., Caplar N., Bellovary J. M., Wang Z. F., 2023, MNRAS, 518, 1880
Cappellari M., 2017, MNRAS, 466, 798
Cappellari M., Emsellem E., 2004, Publ. Astron. Soc. Pac., 116, 138
Charisi M., Bartos I., Haiman Z., Price-Whelan A. M., Graham M. J., Bellm E. C., Laher R. R., Márka S., 2016, MNRAS, 463, 2145
Chelouche D., Daniel E., 2012, ApJ, 747, 62
Chilingarian I. V., Melchior A.-L., Zolotukhin I. Y., 2010, MNRAS, 405, 1409
Cid Fernandes R., Stasińska G., Schlickmann M. S., Mateus A., Vale Asari N., Schoenell W., Sodré L., 2010, MNRAS, 403, 1036
Cid Fernandes R., Stasińska G., Mateus A., Vale Asari N., 2011, MNRAS, 413, 1687
Comparat J. et al., 2022, A&A, 666, 23
Dálya G. et al., 2018, MNRAS, 479, 2374
Danziger I. J., Fosbury R. A. E., Goss W. M., Ekers R. D., 1979, MNRAS, 188, 415
Davis B. L. et al., 2014, ApJ, 789, 124
De Lorenzi F., Hartmann M., Debattista V. P., Seth A. C., Gerhard O., 2013, MNRAS, 429, 2974
de Vaucouleurs G., de Vaucouleurs A., Corwin H. G. Jr, Buta R. J., Paturel G., Fouque P., 1991, Third Reference Catalogue of Bright Galaxies. Springer, New York, NY
den Brok M. et al., 2015, ApJ, 809, 101
Dudik R. P., Weingartner J. C., Satyapal S., Fischer J., Dudley C. C., O'Halloran B., 2007, ApJ, 664, 71
Edri H., Rafter S. E., Chelouche D., Kaspi S., Behar E., 2012, ApJ, 756, 73
Eisenstein D. J. et al., 2011, AJ, 142, 72
Elvis M., Maccacaro T., Wilson A. S., Ward M. J., Penston M. V., Fosbury R. A. E., Perola G. C., 1978, MNRAS, 183, 129
Fabbiano G., Kim D. W., Trinchieri G., 1992, ApJS, 80, 531
Fan X., 1999, AJ, 117, 2528
Fausnaugh M. M. et al., 2018, ApJ, 854, 107
Fausnaugh M. M. et al., 2021, ApJ, 908, 51
Filippenko A. V., Sargent W. L. W., 1989, ApJ, 342, L11
Gilbert E. A. et al., 2020, AJ, 160, 116
Glass I. S., 1981, MNRAS, 197, 1067
Goad L. E., 1979, in Crawford D. L.ed., SPIE Conf. Ser.Vol. 172, Instrumentation in Astronomy III. SPIE, Bellingham, p. 86
Graham A. W., 2007, MNRAS, 379, 711
Graham A. W., Scott N., 2013, ApJ, 764, 151
Graham A. W., Worley C. C., 2008, MNRAS, 388, 1708
Graham M. J. et al., 2015, MNRAS, 453, 1562
Haas M., Chini R., Ramolla M., Pozo Nuñez F., Westhues C., Watermann R., Hoffmeister V., Murphy M., 2011, A&A, 535, A73
Haggard D., Green P. J., Anderson S. F., Constantin A., Aldcroft T. L., Kim D.-W., Barkhouse W. A., 2010, ApJ, 723, 1447
Heckman T. M., Best P. N., 2014, ARA&A, 52, 589
Heinze A. N. et al., 2018, AJ, 156, 241
Heraudeau P., Simien F., 1996, A&AS, 118, 111
Hickox R. C. et al., 2009, ApJ, 696, 891
Hinkle J. T. et al., 2022, ApJ, 930, 12
Hinkle J. T. et al., 2023, MNRAS, 521, 3517
Ho L. C., 2008, ARA&A, 46, 475
Holoien T. W. S. et al., 2019, ApJ, 883, 111
Huber D. et al., 2011, ApJ, 743, 143
Ichikawa K., Ueda J., Bae H.-J., Kawamuro T., Matsuoka K., Toba Y., Shidatsu M., 2019, ApJ, 870, 65
Jacobs B. A., Rizzi L., Tully R. B., Shaya E. J., Makarov D. I., Makarova L., 2009, AJ, 138, 332
Jayasinghe T. et al., 2019, MNRAS, 486, 1907
Jayasinghe T. et al., 2021, MNRAS, 503, 200
Jones D. H. et al., 2009, MNRAS, 399, 683

Karachentsev I. D., Tully R. B., Makarova L. N., Makarov D. I., Rizzi L., 2015, ApJ, 805, 144
Kasliwal V. P., Vogeley M. S., Richards G. T., 2017, MNRAS, 470, 3027
Kauffmann G. et al., 2003, MNRAS, 346, 1055
Kelly B. C., Bechtold J., Siemiginowska A., 2009, ApJ, 698, 895
Kelly B. C., Becker A. C., Sobolewska M., Siemiginowska A., Uttley P., 2014, ApJ, 788, 33
Kewley L. J., Dopita M. A., Sutherland R. S., Heisler C. A., Trevena J., 2001, ApJ, 556, 121
Kewley L. J., Groves B., Kauffmann G., Heckman T., 2006, MNRAS, 372, 961
Kim M. et al., 2007, ApJS, 169, 401
Komossa S., 2006, Mem. Soc. Astron. Italiana, 77, 733
Koo D. C., Kron R. G., 1988, ApJ, 325, 92
Kormendy J., Richstone D., 1995, ARA&A, 33, 581
Kourkchi E. et al., 2020, ApJ, 902, 145
Kozłowski S. et al., 2010, ApJ, 708, 927
Lacerda E. A. D., Sánchez S. F., Cid Fernandes R., López-Cobá C., Espinosa-Ponce C., Galbany L., 2020, MNRAS, 492, 3073
Lacy M. et al., 2004, ApJS, 154, 166
Lantz B. et al., 2004, in Mazuray L., Rogers P. J., Wartmann R., eds, SPIE Conf. Series Vol. 5249, Optical Design and Engineering. SPIE, Bellingham, p. 146
Latimer C. J., Reines A. E., Bogdan A., Kraft R., 2021, ApJ, 922, L40
Laurent O., Mirabel I. F., Charmandaris V., Gallais P., Madden S. C., Sauvage M., Vigroux L., Cesarsky C., 2000, A&A, 359, 887
Lawther D., Vestergaard M., Raimundo S., Koay J. Y., Peterson B. M., Fan X., Grupe D., Mathur S., 2023, MNRAS, 519, 3903
Lewis K. T., Eracleous M., 2006, ApJ, 642, 711
Liu T. et al., 2019, ApJ, 884, 36
McQuillan A., Mazeh T., Aigrain S., 2014, ApJS, 211, 24
MacLeod C. L. et al., 2010, ApJ, 721, 1014
Mahony E. K., Croom S. M., Boyle B. J., Edge A. C., Mauch T., Sadler E. M., 2010, MNRAS, 401, 1151
Makarov D., Prugniel P., Terekhova N., Courtois H., Vauglin I., 2014, A&A, 570, A13
Matt G., Guainazzi M., Maiolino R., 2003, MNRAS, 342, 422
Maza J., Ruiz M. T., González L. E., Wischnjewsky M., Antezana R., 1994, Rev. Mex. Astron. Astrofis., 28, 187
Mendez A. J. et al., 2013, ApJ, 770, 40
Mezcua M., Domínguez Sánchez H., 2020, ApJ, 898, L30
Mishra H. D. et al., 2021, ApJ, 913, 146
Moreno J., Vogeley M. S., Richards G. T., Yu W., 2019, Publ. Astron. Soc. Pac., 131, 063001
Mukai K., 1993, Legacy, 3, 21
Mushotzky R., 2004, How are AGN Found?. Kluwer Academic Publishers, Dordrecht, NL, p. 53
Mutlu-Pakdil B., Seigar M. S., Davis B. L., 2016, ApJ, 830, 117
Oke J. B., Gunn J. E., 1982, Publ. Astron. Soc. Pac., 94, 586
Pacucci F., Mezcua M., Regan J. A., 2021, ApJ, 920, 12
Panzera M. R., Campana S., Covino S., Lazzati D., Mignani R. P., Moretti A., Tagliaferri G., 2003, A&A, 399, 351
Payne A. V. et al., 2021, ApJ, 910, 125
Payne A. V. et al., 2022a, ApJ, 951, 21
Payne A. V. et al., 2022b, ApJ, 926, 142
Pietsch W., Bischoff K., Boller T., Doebereiner S., Kollatschny W., Zimmermann H. U., 1998, A&A, 333, 48
Ptak A., Griffiths R., 2003, in Payne H. E., Jedrzejewski R. I., Hook R. N., eds, ASP Conf. Ser. Vol. 295, Astronomical Data Analysis Software and Systems XII., San Francisco, p. 465
Pulatova N. G., Vavilova I. B., Sawangwit U., Babyk I., Klimanov S., 2015, MNRAS, 447, 2209
Radburn-Smith D. J. et al., 2011, ApJS, 195, 18
Ricci C. et al., 2017, ApJS, 233, 17
Richards G. T. et al., 2001, AJ, 121, 2308
Richings A. J., Uttley P., Körding E., 2011, MNRAS, 415, 2158
Richstone D. et al., 1998, Nature, 385, A14
Ricker G. R. et al., 2014, in Oschmann J. M. Jr, Clampin M., Fazio G. G., MacEwen H. A., eds, SPIE Conf. Ser. Vol. 9143, Space Telescopes and Instrumentation 2014: Optical, Infrared, and Millimeter Wave. SPIE, Bellingham, p. 914320
Riess A. G. et al., 2016, ApJ, 826, 56
Risaliti G., Maiolino R., Bassani L., 2000, A&A, 356, 33
Rodrigo C., Solano E., 2020, in Contributions to the XIV.0 Scientific Meeting (virtual) of the Spanish Astronomical Society, p. 182. Available at: https://www.sea-astronomia.es/sites/default/files/vl_rodrigo_c_1.pdf
Romano P., Campana S., Mignani R. P., Moretti A., Mottini M., Panzera M. R., Tagliaferri G., 2008, A&A, 488, 1221
Ruschel-Dutra D., Rodríguez Espinosa J. M., González Martín O., Pastoriza M., Riffel R., 2017, MNRAS, 466, 3353
Saglia R. P. et al., 2016, ApJ, 818, 47
Saxton R. D., Read A. M., Esquej P., Freyberg M. J., Altieri B., Bermejo D., 2008, A&A, 480, 611
Shappee B. J. et al., 2014, ApJ, 788, 48
Skrutskie M. F. et al., 2006, AJ, 131, 1163
Spinoglio L., Malkan M. A., 1989, ApJ, 342, 83
Stern D. et al., 2012, ApJ, 753, 30
Tadhunter C., 2016, A&A Rev., 24, 10
Theureau G., Hanski M. O., Coudreau N., Hallet N., Martin J. M., 2007, A&A, 465, 71
Thim F., Hoessel J. G., Saha A., Claver J., Dolphin A., Tammann G. A., 2004, AJ, 127, 2322
Tonry J. L. et al., 2018, ApJ, 867, 105
Traulsen I. et al., 2020, A&A, 641, A137
Tremaine S. et al., 2002, ApJ, 574, 740
Trump J. R. et al., 2015, ApJ, 811, 26
Tucker M. A., Huber M., Shappee B. J., Dong S., Bose S., Chen P., 2018, The Astronomer's Telegram, 11444, 1
Tucker M. A. et al., 2021, MNRAS, 506, 6014
Tucker M. A. et al., 2022, Publ. Astron. Soc. Pac., 134, 124502
Tully R. B., Fisher J. R., 1988, Catalog of Nearby Galaxies. Cambridge Univ. Press, Cambridge, UK
Tully R. B., Shaya E. J., Karachentsev I. D., Courtois H. M., Kocevski D. D., Rizzi L., Peel A., 2008, ApJ, 676, 184
Tully R. B., Rizzi L., Shaya E. J., Courtois H. M., Makarov D. I., Jacobs B. A., 2009, AJ, 138, 323
Tully R. B. et al., 2013, AJ, 146, 86
Tully R. B., Courtois H. M., Sorce J. G., 2016, AJ, 152, 50
Turner T. J., Nandra K., Turcan D., George I. M., 2001, in White N. E., Malaguti G., Palumbo G. G. C., eds, AIP Conf. Ser. Vol. 599, X-ray Astronomy: Stellar Endpoints, AGN, and the Diffuse X-ray Background. Am. Inst. Phys., New York, p. 991
Tzanavaris P., Georgantopoulos I., 2007, A&A, 468, 129
Ueda Y., Ishisaki Y., Takahashi T., Makishima K., Ohashi T., 2001, ApJS, 133, 1
Ueda Y., Ishisaki Y., Takahashi T., Makishima K., Ohashi T., 2005, ApJS, 161, 185
Vallely P. J., Kochanek C. S., Stanek K. Z., Fausnaugh M., Shappee B. J., 2021, MNRAS, 500, 5639
Vanderspek R., Doty J. P., Fausnaugh M., Villasenor J. N. S., Jenkins J. M., Berta-Thompson Z. K., Burke C. J., Ricker G. R., 2018, Technical Report, TESS Instrument Handbook, Kavli Institute for Astrophysics and Space Science, Massachusetts Institute of Technology
Veilleux S., Osterbrock D. E., 1987, ApJS, 63, 295
Véron-Cetty M. P., Véron P., 2006, A&A, 455, 773
Vulic N. et al., 2022, A&A, 661, A16
Wang J., Xu D. W., Wang Y., Zhang J. B., Zheng J., Wei J. Y., 2019, ApJ, 887, 15
Ward C. et al., 2022, ApJ, 936, 104
Way Z. S., Jayasinghe T., Kochanek C. S., Stanek K. Z., Vallely P., Thompson T. A., Holoien T. W. S., Shappee B. J., 2022, MNRAS, 514, 200
Webb N. A. et al., 2020, A&A, 641, A136
Westerlund B. E., Stokes N. R., 1966, ApJ, 145, 354

White N. E., Giommi P., Angelini L., 1994, American Astronomical Society Meeting Abstracts. p. 41.11
Williams D. R. A. et al., 2021, MNRAS
Wright E. L., 2006, Publ. Astron. Soc. Pac., 118, 1711
Wright E. L. et al., 2010, AJ, 140, 1868
Xie G.-Z., Chen L.-E., Li H.-Z., Mao L.-S., Dai H., Xie Z.-H., Ma L., Zhou S.-B., 2005, Chinese J. Astron. Astrophys., 5, 463
Yu J., Bedding T. R., Stello D., Huber D., Compton D. L., Gizon L., Hekker S., 2020, MNRAS, 493, 1388
Yu W., Richards G. T., Vogeley M. S., Moreno J., Graham M. J., 2022, ApJ, 936, 132
Yuk H., Dai X., Jayasinghe T., Fu H., Mishra H. D., Kochanek C. S., Shappee B. J., Stanek K. Z., 2022, ApJ, 930, 110
Zeldes J. et al., 2021, preprint (arXiv:2109.04501)
Zimmermann H. U., Boller T., Döbereiner S., Pietsch W., 2001, A&A, 378, 30

SUPPORTING INFORMATION

Supplementary data are available at *MNRAS* online.

hyperleda_sample_sorted_MR.pdf
candidate_light_curves_MR.txt
GLADE_paper_table_names_MR.txt
source_outcomes_names_MR.txt
visual_inspection_names_MR.txt

Please note: Oxford University Press is not responsible for the content or functionality of any supporting materials supplied by the authors. Any queries (other than missing material) should be directed to the corresponding author for the article.

This paper has been typeset from a TEX/LATEX file prepared by the author.